

Stellar feedback in M83 as observed with MUSE

I. Overview, an unprecedented view of the stellar and gas kinematics and evidence of outflowing gas

Lorenza Della Bruna¹, Angela Adamo¹, Philippe Amram², Erik Rosolowsky³, Christopher Usher¹, Mattia Sirressi¹, Andreas Schrubba⁴, Eric Emsellem^{5,6}, Adam Leroy⁷, Arjan Bik¹, William P. Blair⁸, Anna F. McLeod^{9,10}, Göran Östlin¹, Florent Renaud¹¹, Carmelle Robert¹², Laurie Rousseau-Nepton^{13,14}, and Linda J. Smith¹⁵

¹ The Oskar Klein Center, Department of Astronomy, Stockholm University, AlbaNova 10691, Stockholm, Sweden
e-mail: lorenza.dellabruna@astro.su.se

² Aix-Marseille Université, CNRS, CNES, LAM, Marseille, France

³ Department of Physics, University of Alberta, Edmonton AB T6G 2E1, Canada

⁴ Max-Planck-Institut für extraterrestrische Physik, Giessenbachstraße 1, 85748 Garching, Germany

⁵ European Southern Observatory, Karl-Schwarzschild-Str. 2, 85748 Garching, Germany

⁶ Univ. Lyon, Univ. Lyon1, ENS de Lyon, CNRS, Centre de Recherche Astrophysique de Lyon, UMR5574, 69230 Saint-Genis-Laval, France

⁷ Department of Astronomy, The Ohio State University, 140 West 18th Avenue, Columbus, Ohio 43210, USA

⁸ The William H. Miller III Department of Physics and Astronomy, Johns Hopkins University, 3400 N. Charles Street, Baltimore 21218, USA

⁹ Centre for Extragalactic Astronomy, Department of Physics, Durham University, South Road, Durham DH1 3LE, UK

¹⁰ Institute for Computational Cosmology, Department of Physics, University of Durham, South Road, Durham DH1 3LE, UK

¹¹ Department of Astronomy and Theoretical Physics, Lund Observatory, Box 43, 221 00 Lund, Sweden

¹² Département de physique, de génie physique et d'optique, Université Laval, Quebec, Canada

¹³ Canada-France-Hawaii Telescope, Kamuela 96743, USA

¹⁴ Department of Physics and Astronomy, University of Hawaii, Hilo 96720-4091, USA

¹⁵ European Space Agency (ESA), ESA Office, Space Telescope Science Institute, 3700 San Martin Drive, Baltimore 21218, USA

Received 27 September 2021 / Accepted 1 February 2022

ABSTRACT

Context. Young massive stars inject energy and momentum into the surrounding gas, creating a multi-phase interstellar medium (ISM) and regulating further star formation. The main challenge of studying stellar feedback proves to be the variety of scales spanned by this phenomenon, ranging from the immediate surrounding of the stars (H II regions, 10s pc scales) to galactic-wide kiloparsec scales. **Aims.** We present a large mosaic (3.8×3.8 kpc) of the nearby spiral galaxy M83, obtained with the MUSE instrument at ESO Very Large Telescope. The integral field spectroscopy data cover a large portion of the optical disk at a resolution of ~ 20 pc, allowing the characterisation of single H II regions while sampling diverse dynamical regions in the galaxy.

Methods. We obtained the kinematics of the stars and ionised gas, and compared them with molecular gas kinematics observed in CO(2-1) with the ALMA telescope array. We separated the ionised gas into H II regions and diffuse ionised gas (DIG) and investigated how the fraction of H α luminosity originating from the DIG (f_{DIG}) varies with galactic radius.

Results. We observe that both stars and gas trace the galactic disk rotation, as well as a fast-rotating nuclear component ($30'' \approx 700$ pc in diameter), likely connected to secular processes driven by the galactic bar. In the gas kinematics, we observe a stream east of the nucleus ($50'' \approx 1250$ pc in size), redshifted with respect to the disk. The stream is surrounded by an extended ionised gas region (1000×1600 pc) with enhanced velocity dispersion and a high ionisation state, which is largely consistent with being ionised by slow shocks. We interpret this feature as either the superposition of the disk and an extraplanar layer of DIG, or as a bar-driven inflow of shocked gas. A double Gaussian component fit to the H α line also reveals the presence of a nuclear biconic structure whose axis of symmetry is perpendicular to the bar. The two cones ($20'' \approx 500$ pc in size) appear blue- and redshifted along the line of sight. The cones stand out for having an H α emission separated by up to 200 km s^{-1} from that of the disk, and a high velocity dispersion ~ 80 – 200 km s^{-1} . At the far end of the cones, we observe that the gas is consistent with being ionised by shocks. These features had never been observed before in M83; we postulate that they are tracing a starburst-driven outflow shocking into the surrounding ISM. Finally, we obtain $f_{\text{DIG}} \sim 13\%$ in our field of view, and observe that the DIG contribution varies radially between 0.8 and 46%, peaking in the interarm region. We inspect the emission of the H II regions and DIG in ‘BPT’ diagrams, finding that in H II regions photoionisation accounts for 99.8% of the H α flux, whereas the DIG has a mixed contribution from photoionisation (94.9%) and shocks (5.1%).

Key words. galaxies: general – galaxies: individual: NGC 5236 – galaxies: ISM – galaxies: kinematics and dynamics – ISM: structure – H II regions

1. Introduction

Young massive stars originate from the gravitational collapse of giant molecular clouds (GMCs), and they inject energy and

momentum into the surrounding interstellar medium (ISM) via different feedback processes such as thermal feedback from protostars, photoionisation, and mechanical feedback from stellar winds and supernovae (for a review, see [Krumholz et al. 2014](#)

and Dale 2015). These combined effects can disrupt the parent GMCs (Dale 2015; Howard et al. 2017), resulting in a self-regulating mechanism which inhibits future star formation. On the other hand, positive feedback can occasionally facilitate further collapse in neighbouring regions, boosting the formation of new stars. Stellar feedback directly affects star-forming regions by carving channels and ‘bubbles’ of ionised gas into the surrounding cool gas and dust, and it also impacts the ISM on wider galactic scales, as it clears the path for winds and outflows to escape the star-forming regions. Overall, stellar feedback can shape the global properties of a galaxy (e.g., Scannapieco et al. 2012; Hopkins et al. 2013), and it plays a key role in the recycling of gas, the regulation of star formation, and the chemical enrichment and mixing of star-forming galaxies (e.g., Leroy et al. 2015a; Maiolino & Mannucci 2019). Modelling feedback has therefore proven to be essential in simulations of GMCs (e.g., Dale et al. 2014) as well as galaxy formation and evolution (Schaye et al. 2015; Hopkins et al. 2018) in order to correctly reproduce key observables and relations between them.

A more detailed understanding of the process of stellar feedback is also key to explain the origin of a warm and diffuse component of the ISM (diffuse ionised gas or DIG, see Haffner et al. 2009 for a review), which has been observed to make up a considerable fraction of the H α emission (up to 50%) in local spiral galaxies (Ferguson et al. 1996; Zurita et al. 2000; Thilker et al. 2002; Hoopes & Walterbos 2003; Oey et al. 2007). The origin of this ISM component is still under study, and has been linked to radiation leaking from the star-forming regions (Zurita et al. 2002; Weilbacher et al. 2018; Belfiore et al. 2022; Della Bruna et al. 2021), field stars (Hoopes & Walterbos 2000; Zhang et al. 2017; Belfiore et al. 2022), shocks (Collins & Rand 2001), cosmic rays (Vandenbroucke et al. 2018) or scattering by dust (Seon & Witt 2012). Studying stellar feedback in nearby galaxies will allow to probe the role of each of these processes in ionising the DIG.

The advent of integral field spectroscopy (IFS) has been a leap forward in the study of stellar feedback, as it allows to acquire spectral information of multiple lines simultaneously over a relatively wide field of view (FoV) at good angular resolution. This makes it possible for example to obtain at the same time the kinematics of gas and stars, and to disentangle different gas ionisation mechanisms (see Kewley et al. 2019, for a review).

IFS instruments have led the way to multi-scale studies of kinematics and physical properties of ionised gas in nearby galaxies. At the largest (kpc) scales, surveys such as CALIFA (Sánchez et al. 2012), MANGA (Bundy et al. 2015) and SAMI (Croom et al. 2012; Bryant et al. 2015) provided a census of the $z \sim 0$ galaxy population. The large sample of H II regions provided by these surveys allowed for a better understanding of the general properties of star forming regions. For example, it was possible to investigate the link between the physical conditions of the ISM and the stellar population in the regions (Sánchez et al. 2015), and between the stellar population and the leakage of ionising photons (Morisset et al. 2016). Large scale surveys also allowed to quantify and characterise the presence of extraplanar DIG (eDIG) in edge-on spiral galaxies (Bizyaev et al. 2017; Jones et al. 2017; Levy et al. 2019).

At intermediate scales, two instruments whose wide field coverage and high sensitivity have been particularly important for the study of feedback are: the MUSE integral field unit (IFU, Bacon et al. 2010), mounted on the ESO Very Large Telescope (VLT) at Cerro Paranal observatory and the SITELLE imaging fourier transform spectrograph at Canada-France-Hawaii Tele-

scope (CFHT, Drissen et al. 2019). The relatively large FoV (1 arcmin² and 11 \times 11 arcmin², respectively) and high spatial sampling (0''.2 and 0''.32 pixel⁻¹) of these instruments are ideal to study global properties of nearby galaxies, while at the same time achieving a high level of detail at small scales. This was exploited by galaxy surveys such as MAD (Erroz-Ferrer et al. 2019; den Brok et al. 2020), SIGNALS (Rousseau-Nepton et al. 2019) and PHANGS-MUSE (Emsellem et al. 2022), that are targeting each ~ 20 –50 galaxies, at distances where 1'' ~ 50 –200 pc, enabling the identification and characterisation of individual H II regions. This makes it possible to study the dependence of region properties on their location in the galaxy (e.g., in arm vs. inter-arm regions) and on the local ISM conditions (Kreckel et al. 2016, 2019; Erroz-Ferrer et al. 2019).

Finally, a few specific studies of local galaxies with MUSE (LMC, McLeod et al. 2019; NGC 300, McLeod et al. 2020, 2021; NGC 7793, Della Bruna et al. 2020, 2021) are starting to probe scales of tens of parsec, resolving individual H II regions in detail and detecting the most massive individual stars, which gives a way to bridge small and galaxy-scale stellar feedback. For individual regions, this allows one to investigate, for example, the contribution of various types of feedback (McLeod et al. 2019, 2020, 2021), the ionisation structure of the region and to derive an escape fraction by modelling the expected ionising photon flux based on the observed stellar population (McLeod et al. 2019, 2020; Della Bruna et al. 2020, 2021).

In this study, we exploit MUSE IFS data to study the ISM in the nearby galaxy M83 at a scale of ~ 20 pc. Our work complements the very high resolution (10 pc) studies and the large scale (100 pc – kpc) studies, by covering a wide area (~ 20 arcmin²) at a resolution that still allows the characterisation of individual H II regions while at the same time sampling a large number of regions (~ 4700 , Della Bruna et al., in prep.) and a wide range of ISM conditions across the galactic disk.

M83 (also known in the literature as NGC 5236) is a nearby spiral galaxy, at a distance of 4.89 Mpc (Jacobs et al. 2009). Figures 1 and 2 show M83 observed with the *Hubble* Space Telescope (HST) and the Atacama Large Millimeter/submillimeter Array (ALMA), and with MUSE (this work). M83 has a grand design barred spiral morphology, and its full optical disk is ~ 20 kpc across; the position of the stellar bar and the two spiral arms¹ are sketched in Fig. 1. The galaxy has a stellar mass $\log_{10} M_{\star} = 10.53 M_{\odot}$ (Leroy et al. 2021b) and hosts a nuclear starburst ring (Sérsic & Pastoriza 1965; Buta & Crocker 1993; Calzetti et al. 2004; Comerón et al. 2010; Knapen et al. 2010), resulting in a high star formation rate (SFR = 4.2 $M_{\odot} \text{ yr}^{-1}$, Leroy et al. 2021b). Its offset from the SFR- M_{\star} main sequence for star forming galaxies ($\Delta_{\text{MS}} = 0.44$ dex) is consistent with the typical scatter at this stellar mass (Popesso et al. 2019). M83 has been extensively studied over all wavelengths, and its stellar population has been mapped across the galactic disk. Catalogues of young star clusters (YSCs, Silva-Villa et al. 2014; Adamo et al. 2015), Wolf-Rayet stars (Hadfield et al. 2005) and supernova remnants (Blair et al. 2014; Winkler et al. 2017; Williams et al. 2019; Russell et al. 2020) are publicly available. Overall, this makes M83 an ideal candidate for the detailed study of stellar feedback at scales of 10 s of parsecs.

¹ We determine the outline of spiral arms as the inner radius of the star-forming regions identified in Sect. 5, and the bar position angle based on archival *Spitzer* S⁴G data (Sheth et al. 2010; Salo et al. 2015, <https://irsa.ipac.caltech.edu/data/SPITZER/S4G/galaxies/NGC5236.html>).

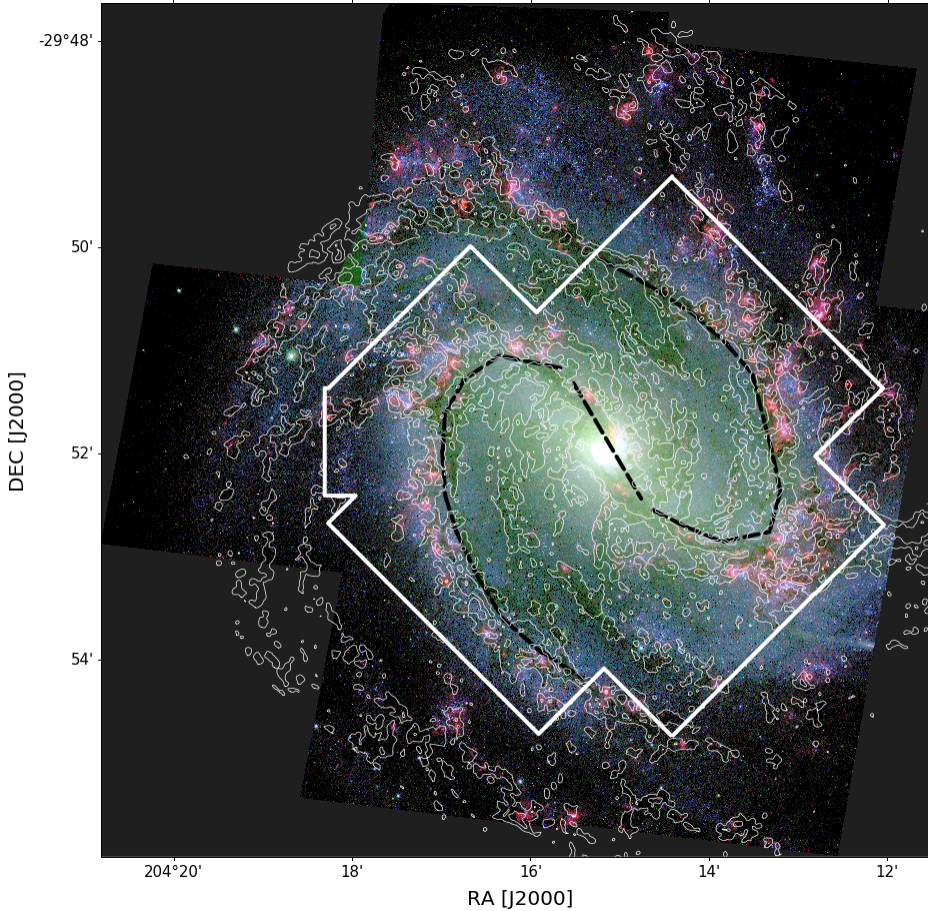


Fig. 1. HST colour-composite image of M83 (Red: F657N, Blue: F814W, Green: F438W). The footprint of the MUSE mosaic is overlaid in white. The position of the bar and the two spiral arms is sketched in black (see Sect. 1). The white contours trace molecular gas mass surface density from ALMA CO(2-1) (contours of 5 and 25 K km s⁻¹, corresponding to a surface gas density ≈ 30 and $170 M_{\odot} \text{pc}^{-2}$).

The MUSE data presented in this work consist of a large mosaic covering the central 3.8 kpc in radial extent at ~ 20 pc resolution. This is the first extensive IFS study of stars and ionised gas across the disk of M83. Previous studies have either targeted the ionised gas using a wide field spectrograph (Poetrodjojo et al. 2019, ~ 40 pc resolution) or Fabry–Pérot observations (Fathi et al. 2008), or have focused on spectroscopy of the nuclear region (e.g., Knapen et al. 2010; Piqueras López et al. 2012; Gadotti et al. 2020; Callanan et al. 2021). We complement our observations with high-resolution archival imaging from HST (< 2 pc resolution) and CO(2-1) observations from ALMA at ~ 50 pc resolution. An overview of the dataset is shown in Fig. 1. The MUSE data allow us to map for the first time the large-scale stellar kinematics, as well as unprecedentedly detailed H α kinematics. The wealth of information provided by IFU spectroscopy enables us to investigate spatially resolved physical properties of the gas. At the same time, the HST coverage provides us with a detailed catalogue of massive stars and clusters, and the ALMA data trace the distribution of the molecular gas in the galaxy. The goal of this project is the study of star formation from galactic scales (this paper) to small scale (~ 20 pc, Della Bruna et al., in prep.). The data allow also for a census of Wolf-Rayet stars (Smith et al., in prep.), planetary nebulae (Della Bruna et al., in prep.) and supernova remnants (Long et al., in prep.). Ultimately, we aim to provide a comprehensive picture of the star formation cycle in M83 at tens of parsec scales.

This paper is organised as follows: in Sect. 2 we give an overview of the dataset and of the MUSE data reduction. In Sect. 3 we present the kinematics of stars and ionised gas. In

Sect. 4 we estimate the extinction from the ionised gas and compare it with the distribution of the molecular gas. In Sect. 5 we identify H II regions complexes, determine the fraction of DIG and inspect the properties of the ionised gas in emission line diagrams. In Sect. 6 we take a closer look at the kinematics and emission of the central starburst region. Finally, in Sects. 7 and 8 we discuss the results and draw our conclusions.

2. Dataset overview and MUSE data reduction

We observed M83 with the MUSE instrument at VLT (observing programmes 096.B-0057(A) and 0101.B-0727(A), PI Adamo). The main properties of the target are summarised in Table 1. The MUSE data cover the inner ~ 3.8 kpc in galactocentric radial extent ($1.1 \times R_e$ in effective radius, see Table 1), and a total physical area of 40.5 kpc^2 . The dataset consists of 20 pointings (indicated in green in the top panel of Fig. C.1) in Wide Field Mode (WFM) and extended wavelength configuration (4650–9300 Å), for a total of 46 exposures. The pointings were observed with science exposures of 550 s (4 exposures for pointings 1 to 8, a single exposure for remaining pointings). Sky frames of 180 s were obtained such that every science exposure is preceded or followed by a sky frame acquisition. Because of the large extent of the target in the sky, sky frame offsets were larger than 4 arcmin. We complemented our observations with MUSE data available in the ESO archive: observing programmes 097.B-0899(B) (PI Ibar) and 097.B-0640(A) (PI Gadotti). Both programmes were observed in WFM with nominal wavelength range (4800–9300 Å). From these programmes, we excluded some frames

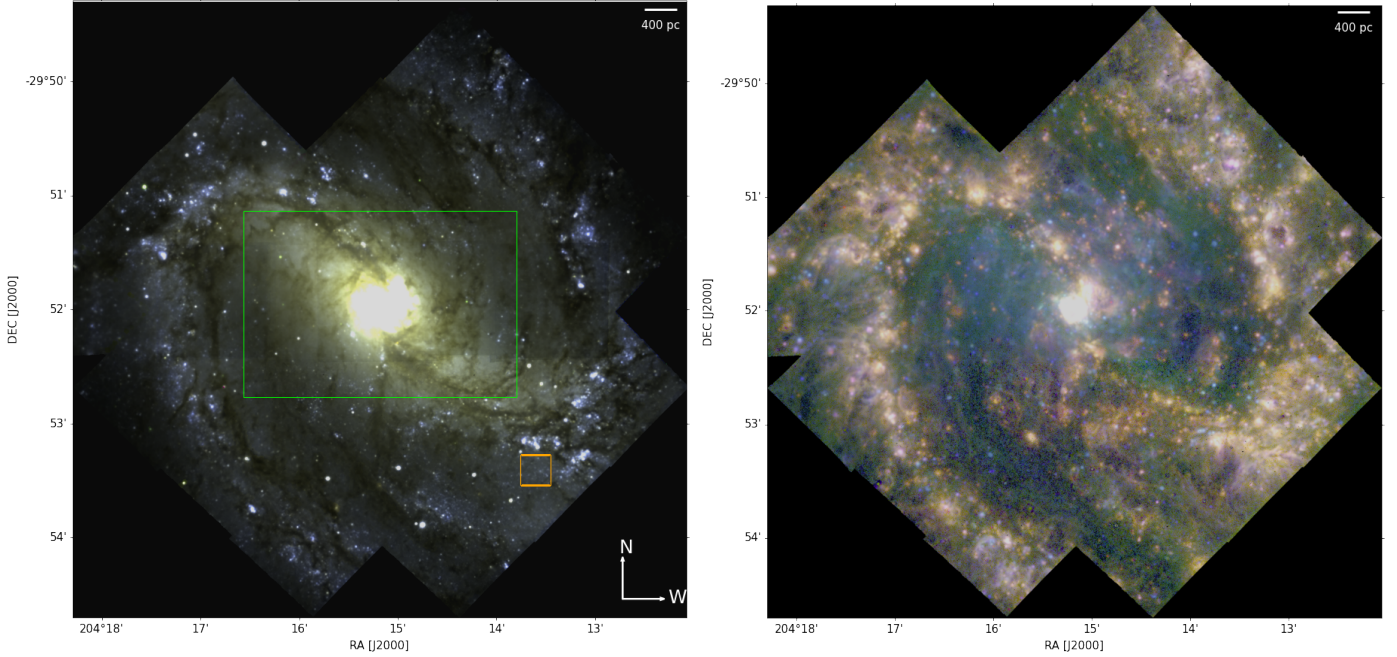


Fig. 2. Three-colour composites of the MUSE data. *Left:* composite of stellar bands (Blue: 4875–4950 Å, Green: 6520–6528 Å, Red: 6750–6810 Å). The green rectangle indicates the central starburst region analysed in Sect. 6. The orange square indicates the position of the $H\alpha$ cloud highlighted in Fig. 3 (central panels). *Right:* composite of gas emission (Blue: [O III], Green: [S II], Red: $H\alpha$).

that had calibration issues, poor seeing or that were not fully overlapping with the rest of our dataset. From archival dataset 097.B-0899(B) we included five pointings (indicated in blue in Fig. C.1, top panel), each observed during three science exposures of 600 s with two external sky frames with a 180 s exposure. Archival dataset 097.B-0640(A) consists of one pointing (purple square in Fig. C.1, top panel), of which we included four 480 s exposures, and an additional two sky exposures of 300 s.

The final mosaic consists of 26 pointings for a total of 65 MUSE exposures. The central coordinates and exposure time of all the included pointings can be found in Appendix C (Table C.1 and Fig. C.1). The pointings were imaged over a wide range of observing conditions. We derived a PSF for each pointing by fitting a Moffat profile as a function of wavelength to bright, isolated point sources with PAMPELMUSE (Kamann 2018), and report the values in Table C.1. Across the full mosaic we measure a median PSF of $0''.7$ at 7000 \AA (17 pc at the distance of our target). The full width at half maximum of the Moffat profile declines with increasing wavelength, with a median difference of $0''.16$ between the blue and red end.

M83 was also observed with HST during the WFC3 Early release science programme (GO11360, PI O’Connell), using narrow and broad band imaging ranging from the UV to the NIR. The coverage of the inner 4.5 kpc ($1.3 \times R_e$) in galactocentric radius was later completed with the programme GO12513 (PI Blair). In total, the HST mosaic consists of seven contiguous pointings (Blair et al. 2014), with a $FWHM \sim 0''.08$ (1.9 pc).

Finally, archival ALMA CO ($J=2-1$) data² covering the inner 7.2 kpc ($2.1 \times R_e$) of the galaxy in galactocentric radius have been processed as part of the PHANGS-ALMA survey (Leroy et al. 2021b) using the PHANGS-ALMA pipeline (Leroy et al. 2021a). The data have an angular resolution of $2''.14$ (50 pc), a spectral resolution of $2.5 \text{ km s}^{-1} \text{ channel}^{-1}$ and a rms brightness

Table 1. Physical properties of M83.

	Parameter	Value	Ref.
Distance and morphology	Distance	4.89 Mpc ($1'' = 24 \text{ pc}$)	(1)
	Effective radius	3.5 kpc	(2)
	Morphological Type	SAB(s)c	(3)
Physical properties	$\log_{10} M_*$	$10.53 M_\odot$	(2)
	SFR	$4.2 M_\odot \text{ yr}^{-1}$	(2)
	$\Delta_{\text{MS}}^{(a)}$	0.44 dex	(2)
	$\log_{10} \tau_{\text{dep}}^{\text{mol} (b)}$	8.9 yr	(2)
	Central abundance	$12 + \log(\text{O}/\text{H}) = 8.99$	(4)

Notes. ^(a)Offset from the SFR- M_* main sequence. ^(b)Derived assuming $\log_{10} L_{\text{CO}} = 8.84 \text{ K km s}^{-1} \text{ pc}^{-2}$ (Leroy et al. 2021b), a standard Galactic $\alpha_{\text{CO}} = 4.35 M_\odot \text{ pc}^{-2} (\text{K km s}^{-1})^{-1}$ and $R_{21} = 0.65$ (den Brok et al. 2021; Leroy et al. 2022).

References. (1) Jacobs et al. (2009); (2) Leroy et al. (2021b); (3) RC3 catalogue (de Vaucouleurs et al. 1991; Buta et al. 2015); (4) Bresolin et al. (2016).

temperature sensitivity of 0.17 K. The data are described in detail in Leroy et al. (2021b), and the data reduction in Leroy et al. (2021a).

In Fig. 1 we show a 3-colour composite of the HST data. The footprint of the MUSE mosaic is shown in white. The white contours indicate the ALMA CO emission at levels of 5 and 25 K km s^{-1} . Using Eq. (1) in Sun et al. (2020) and assuming a CO(2-1)-to-CO(1-0) line ratio $R_{21} = 0.65$ (den Brok et al. 2021; Leroy et al. 2022) and a standard Galactic CO-to-H₂ conversion factor $\alpha_{\text{CO}} = 4.35 M_\odot \text{ pc}^{-2} (\text{K km s}^{-1})^{-1}$, these values corresponds to a cold gas surface density of ≈ 30 and $170 M_\odot \text{ pc}^{-2}$. The position of the bar and the spiral arms is shown with black dashed lines (see Sect. 1). The HST and ALMA data cover the inner ~ 4.5 –7 kpc of the disk, imaging the spiral arms in their entirety, whereas the MUSE mosaic is limited to the central 3.8 kpc.

² Project codes 2013.1.01161.S, 2015.1.00121.S and 2016.1.00386.S, PI Sakamoto.

We reduced the MUSE data with the ESO pipeline (Weilbacher et al. 2014, 2020, v2.8.3), following the standard reduction procedure. In a first phase, the instrumental signature was removed using `muse_scibasic`. For this purpose, we combined bias frames to account for the readout noise and lamp frames to correct for flat fielding. Wavelength calibration was performed by combining arc-lamp frames, and correction of 3D illumination and a refined flat-fielding was achieved by combining twilight frames. Moreover, we used the line spread function (LSF) and geometry table (describing the spatial location of IFU slicers) distributed with the pipeline. In a second phase, we performed flux calibration using a standard star, and we modelled the sky spectrum from the sky frames with `muse_create_sky`. We then ran `muse_scipost` on the object and sky frames. For the object frame, we used the ‘subtract-model’ sky subtraction method, that uses sky lines and continuum estimated from the sky frames. We saved whitelight images as well as individual pixel table, that we later used when aligning and combining the individual exposures. In a third step, we assembled the final mosaic. We used `muse_exp_align` to compute offsets between multiple exposures of the same pointing. Offsets between different pointings were instead computed by matching each MUSE whitelight image with the *B*-band HST mosaic obtained from the MAST archive³, and registered to the *Gaia* DR2 (Gaia Collaboration 2018). We selected in each MUSE image at least ten point-like sources within the FOV that corresponded to isolated bright clusters in the HST frame. The list of offsets in WCS was then used by `muse_exp_combine` to combine the individual pixel tables into a large mosaic. A colour composite of the stellar continuum in different broad bands (left) and of three line emission maps (right) extracted from the final MUSE mosaic are shown in Fig. 2.

3. Kinematics of stars and gas

3.1. Stellar kinematics

We fitted the stellar continuum with PPXF (Cappellari & Emsellem 2004; Cappellari 2017), using the E-MILES simple stellar populations models (Vazdekis et al. 2016) with an unimodal IMF and Padova 2000 isochrones (Girardi et al. 2000). The data are spatially binned using the weighted adaptation (Diehl & Statler 2006) of the Voronoi tessellation method (Cappellari & Copin 2003). The bins were targeted to a signal to noise ratio (S/N) ≈ 250 in the continuum range 5025–5065 Å, corresponding to a $S/N \approx 40 \text{ \AA}^{-1}$. We fitted the range 4600–8740 Å (in order to include the Ca II triplet). All relevant emission lines, as well as sky residuals were masked during the fit; in particular, we excluded entirely the range 7220–8507 Å due to the strong residual sky emission. We used the Gaussian parametrisation of the instrumental LSF by Guérou et al. (2017)⁴. We note that following this parametrisation, velocity dispersions below $\sim 50 \text{ km s}^{-1}$ at $H\alpha$ are undersampled by the MUSE instrument.

The resulting stellar velocity and dispersion maps are shown in Fig. 3 (top row). We observe that the stars exhibit overall a regular rotation, and that the velocity dispersion increases from $\sigma \approx 30 \text{ km s}^{-1}$ in the outskirts to $\sigma \approx 80 \text{ km s}^{-1}$ towards the centre. At the very centre, we observe a fast rotating component and a dip in the velocity dispersion ($\sigma \approx 50 \text{ km s}^{-1}$). We discuss

this feature in Sect. 6.1, where we analyse the kinematics of the starburst region.

3.2. Ionised gas kinematics

We created a stellar continuum subtracted cube (‘gas cube’) by rescaling the best stellar population fit from PPXF in each Voronoi bin by the height of the continuum in each spatial pixel (spaxel). We studied the kinematics of the ionised gas from the $H\alpha$ emission line, the brightest line in the MUSE spectral range throughout our FoV. We Voronoi binned the gas cube to a $S/N \sim 20$ in $H\alpha$ ⁵ and fitted the line with a single Gaussian profile. We used the python `scipy` module `curve_fit`, with an initial guess $(v_i, \sigma_i) = (v_{\text{sys}}, 20) \text{ km s}^{-1}$ for the velocity and velocity dispersion, where v_{sys} is the systemic velocity estimated from the stellar kinematics. We set the initial flux f_i to the integral of the binned spectrum in a window of width 22 Å ($\pm 500 \text{ km s}^{-1}$) centred on the line. We then performed the fit in the same wavelength window, in order to avoid being affected by a poorly subtracted stellar continuum. We constrained $f \geq 0$ and $\sigma \geq 1 \text{ km s}^{-1}$, and leave all other parameters free. We removed the instrumental signature using the parametrisation of the MUSE LSF described in Sect. 3.1. The resulting velocity and dispersion maps are shown in Fig. 3 (middle row panels). We remark that while the spectral resolution of MUSE at $H\alpha$ is coarse ($\sigma_{H\alpha} \approx 120 \text{ km s}^{-1}$), the S/N on the $H\alpha$ line yields a median centroiding accuracy of $\approx 2 \text{ km s}^{-1}$. We also note that the artefacts in both maps are arising from minute calibration uncertainties at the scale of a few 10 s of km s^{-1} and to undersampling of the MUSE LSF (see Sect. 3.1).

The kinematics of the ionised gas are more complex than the stellar kinematics. At galactic scales, we observe an overall disk rotation, while the velocity dispersion increases in the interarm regions ($\sigma \approx 80 \text{ km s}^{-1}$) with respect to the star-forming regions along the spiral arms ($\sigma \approx 20 \text{ km s}^{-1}$). The black square in the central panels of Fig. 3 indicates a compact region that features a peculiar $H\alpha$ velocity which appears to be 100 km s^{-1} lower than the surrounding disk rotation, and a high velocity dispersion $\sim 80 \text{ km s}^{-1}$. Given that this region does not stand out in the stellar RGB image (see orange square in Fig. 2) and that it shows a typical spectrum of a low-luminosity $H\alpha$ region, we interpret it as a cloud of extraplanar gas, possibly falling into or being ejected from the galactic disk.

We also performed a double Gaussian component fit to the $H\alpha$ line. A double component can better capture the emission in the case of extreme line broadening on top of a single emission line peak (caused e.g., by shocks or unresolved flows) and in the case where the line has a double-peaked profile, tracing gas motions on top of the galactic rotation (e.g., resolved flows). The fit was performed as following: in a first step, we fitted a single component, as described above. This fit was then adopted as initial guess for the first component, whereas for the second component, we set an initial guess $(v_i, \sigma_i) = (v_{1\text{comp}}, \sigma_{1\text{comp}})$ and $f_0 = 0.25 \times f_{1\text{comp}}$. All boundary conditions were the same as described above. In order to prevent over-fitting by the broad component (e.g., in the case of a noisy or poorly subtracted continuum), we limited the fit to a window of width 22 Å ($\pm 500 \text{ km s}^{-1}$) around the rest wavelength of $H\alpha$. We determined the optimal number of parameters based on the Bayesian information criterion (BIC) statistic (Schwarz 1978), following the approach of Koch et al. (2021). The BIC statistic consists of a

³ <https://archive.stsci.edu/prepds/m83mos/>

⁴ $FWHM_{\text{LSF}}[\text{\AA}] = 6.266 \times 10^{-8} \lambda^2 - 9.824 \times 10^{-4} \lambda + 6.286$.

⁵ Throughout this work, we estimate the S/N of Voronoi maps using a window of 10 Å centred on λ_{obs} .

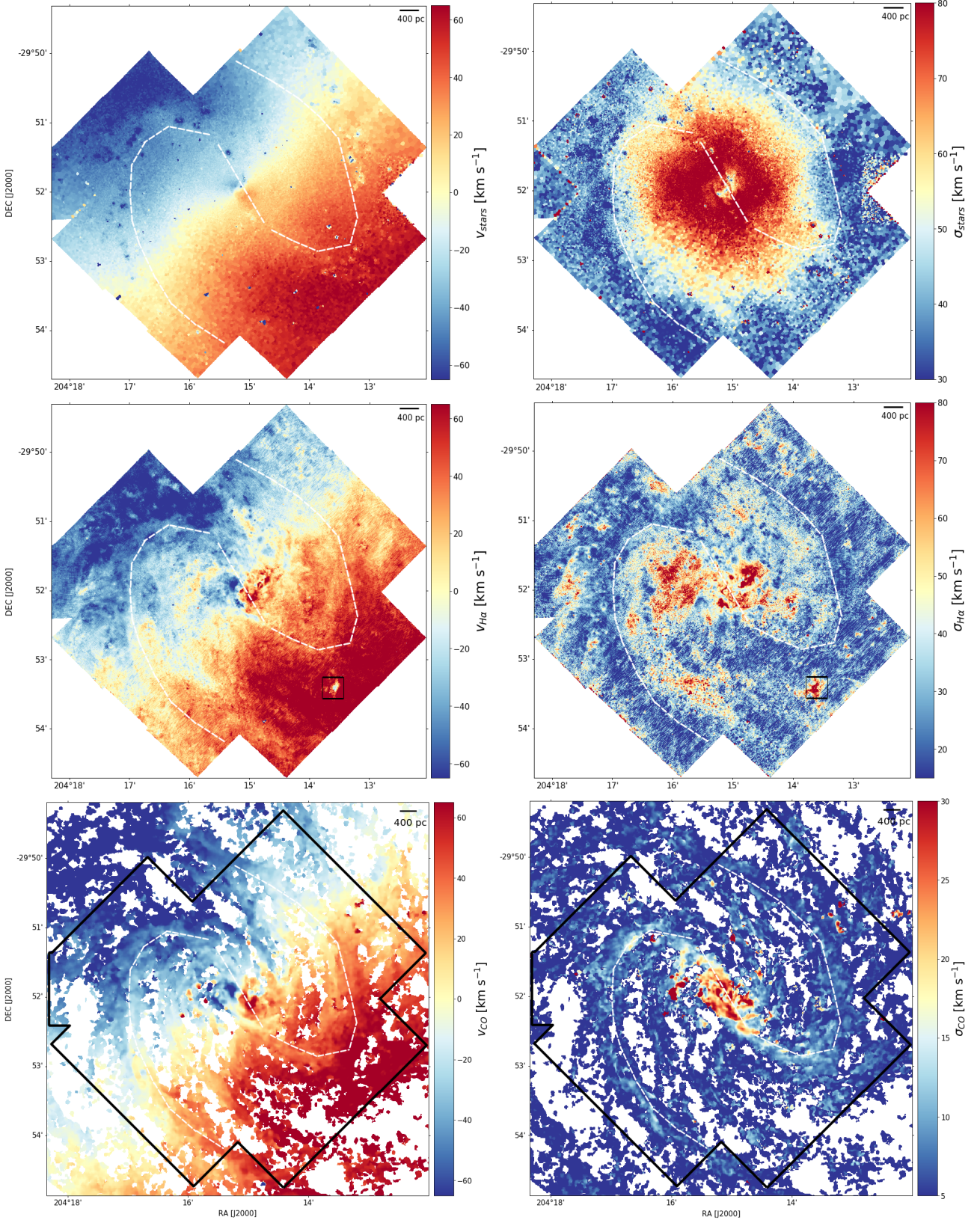


Fig. 3. Kinematics of the stars and gas. *Top row:* MUSE stellar kinematics. *Centre row:* MUSE $H\alpha$ kinematics. The black box in the bottom right corner indicates the position of what we interpret as an extraplanar $H\alpha$ cloud. *Bottom row:* molecular gas kinematics from ALMA CO(2-1) (mom1 and mom2 maps). The footprint of the MUSE data is overlaid in black. All velocity maps have been corrected for systemic velocity; no inclination correction has been applied. The velocity dispersion maps refer to the intrinsic dispersion (instrumental effects have been removed). The white dashed lines sketch the position of the bar and spiral arms as shown in Fig. 1 (see Sect. 1). A zoom-in into the central kinematics is shown in Fig. 11.

Table 2. Parameters derived from the kinematic fitting described in Sect. 3.4.

Model	Stellar component				H α component					CO component		
	(A)	(B)	(C)	(D)	(a)	(b)	(c)	(d)	(e)	(α)	(β)	(γ)
χ_r^2 ⁽¹⁾	1.21	1.23	1.27	1.36	43.7	44.2	46.7	44.6	46.9	1836	1870	2007
<i>incl</i> ⁽²⁾ [°]	20.3	20.0	20.1	19.9	37.9	20.3	20.3	20.3	20.3	35.0	20.3	20.3
v_{sys} ⁽³⁾ [km s ⁻¹]	514.2	513.4	513.0	512.8	513.8	513.9	518.0	513.3	516.1	512.7	512.5	512.9
x_c ⁽⁴⁾ [α_{2000} / arcsec]	13:37:00.43	+3.7	+4.6	+9.4	+0.7	+0.7	+2.0	0	0	+2.8	-1.6	0.0
y_c ⁽⁵⁾ [δ_{2000} / arcsec]	-29:51:56.2	-1.0	-0.8	-4.8	+2.0	+2.0	-6.5	0	0	+3.0	-1.8	0.0
<i>PA</i> ⁽⁶⁾ [°]	223.1	223.0	223.0	222.9	225.8	225.8	225.9	225.8	225.9	225.0	225.0	224.8
ΔV_{rot} ⁽⁷⁾ [km s ⁻¹]	-1.4	0.0	0.9	1.6	5.9	9.8	0	10.7	0	-1.6	-2.1	-2.3

Notes. ⁽¹⁾Reduced χ^2 obtained in fitting the velocity model to the observed velocity field. ⁽²⁾Galaxy inclination. ⁽³⁾Heliocentric systemic LoS velocity. ^(4,5)For Col. (A), right ascension α and declination δ of the kinematic centre. For the next columns: shift in α and δ (in arcsec) from the reference centre given in Col. (A). ⁽⁶⁾Position angle of the major axis of the velocity field. ⁽⁷⁾Mean velocity difference between both sides of the rotation curve. The parameters framed in a box are those that are fixed for the fit. ^(A)Best Fit Model, all nine parameters are free to vary: five parameters for the disk (*incl*, v_{sys} , x_c , y_c and *PA*) and four for the two 2D-Plummer functions (not shown). ^(B)All the parameters are free, except x_c and y_c that are fixed to the centre of the yellow box in Fig. A.3 (i.e. the kinematic centre from Fabry-Perot data, Fathi et al. 2008). ^(C)All the parameters are free, except x_c and y_c that are fixed to the centre of the grey box in Fig. A.3 (i.e. the Pa β kinematic centre, Knapen et al. 2010). ^(D)All the parameters are free, except x_c and y_c that are fixed to the grey cross in Fig. A.3 (i.e. the corner of the errorbox given by Knapen et al. 2010 that is the furthest away from the centre determination obtained in model (A)). ^(a)Same as model (A). ^(b)All the parameters are free, except *incl* (fixed to the value of stellar component). ^(c)All the parameters are free, except *incl* (fixed to the value of stellar component) and ΔV_{rot} (fixed to 0). ^(d)All the parameters are free, except *incl*, x_c and y_c (fixed to the value of stellar component). ^(e)Same as (d), except $\Delta(V_{\text{rot}})$ that is fixed. ^(α)Same as model (A). ^(β)All the parameters are free, except *incl* (fixed to the value of stellar component). ^(γ)All the parameters are free, except *incl*, x_c and y_c (fixed to the value of stellar component).

likelihood term \mathcal{L} plus an additional term that penalises models with more free parameters, and helps preventing overfitting:

$$\text{BIC} = \ln(m)k - 2 \ln(\mathcal{L}). \quad (1)$$

Here, m is the number of fitted data points and k is the number of free parameters. We selected the fit minimising the BIC statistic; we furthermore ignored double component fits in which one component contributes to less than 5% of the total flux. We separated the resulting components into a first component, tracing the galactic rotation, and a second component having a blue or redshift with respect to the disk. In the case where the two components are closer in velocity than 57 km s⁻¹ (corresponding to the MUSE spectral sampling of 1.25 Å at $\lambda_{\text{H}\alpha}$), we picked as the first component the one with the largest amplitude. We found that a double component Gaussian improves the fit only in the starburst region (black rectangle in the left panel of Fig. 2); we therefore present and discuss the resulting kinematic maps in Sect. 6.1, where we study in detail the central kinematics.

3.3. Molecular gas kinematics

In Fig. 3 (bottom row) we show the kinematics of the molecular gas observed in CO(2-1) emission with ALMA. We selected the mom1 and mom2 data obtained with the high confidence ‘strict’ mask (see Leroy et al. 2021a). Despite the difference in resolution, we observe that the molecular gas velocity compares well with the velocity of the ionised gas (centre left panel in Fig. 3). The velocity dispersion is very low (<15 km s⁻¹) throughout the disk, as expected for the cold gas component, and is only enhanced (~25–30 km s⁻¹) around the starburst region. We discuss the kinematics of the central starburst region in Sect. 6.1.

3.4. Kinematic fitting

In order to derive the global kinematic parameters of M83, we fitted the velocity maps of stars and gas with the 2D fitting method described in Epinat et al. (2008) and based on the

Levenberg-Marquardt non-linear least-square algorithm. In our work, the method has been upgraded using the MocKinG software⁶ to take into account uncertainties on the line of sight (LoS) velocities, the flux distribution, the linewidth of the profiles and the spatial resolution.

3.4.1. Analysis of the stellar velocity field

We fitted the raw stellar LoS velocity field with several two-dimensional theoretical velocity distributions, and found that the best fit is obtained using two Plummer components (Plummer 1911), one describing the galactic disk and the other tracing the central structure. The Plummer density profile has a finite density core and falls off as r^{-5} at large radii; this very steep fall-off was essential to fit at best the central component.

The velocity field is described by nine free parameters (see Table 2). They consist of four geometrical parameters – the disk inclination (*incl*), the position angle of the major axis (*PA*), the location of the kinematic centre (x_c , y_c) – plus the heliocentric systemic velocity of the galaxy (v_{sys}). Additionally, each Plummer component has two free parameters which describe the velocity amplitude and the turnover radius, accounting for four other free parameters. We used an angular sector of inclusion of 67.5 degrees (in the galaxy plane) around the major axis⁷, and the LoS velocities were weighted according to their angular distance to the major axis by a cosine function, in order to minimise the contamination due to the predominance of radial motions around the minor axis. Regardless of the initial values for the nine parameters, the best fit model converged towards the same solution (model (A) presented in Table 2). We assessed the robustness of the fit by masking low-S/N regions in the velocity map using Kernel filters, testing various several S/N thresholds (see also Appendix A). We found that even when reducing by

⁶ <https://gitlab.lam.fr/bepinat/MocKinG>.

⁷ The reason for this choice is the fact that the LoS velocities along and close to the minor axis are dominated by radial motions (expansion and contraction along the radius) rather than by galactic rotation.

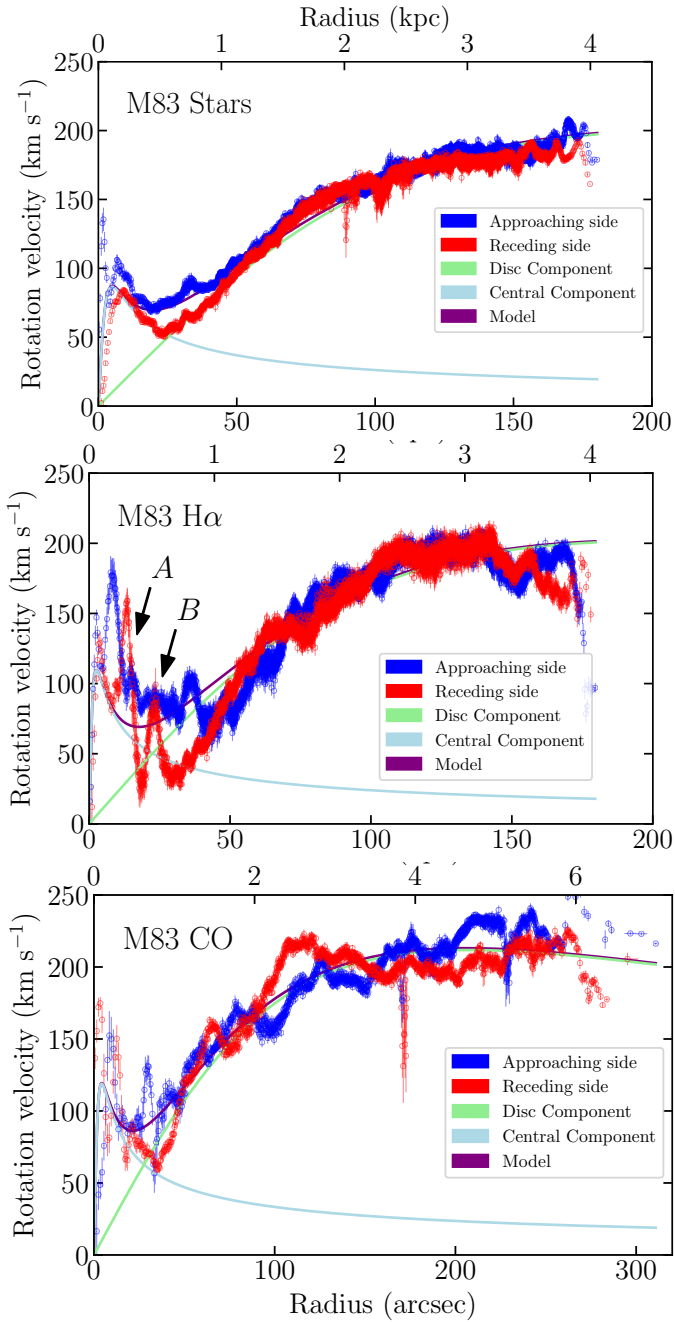


Fig. 4. Rotation curves for the stellar (*top*), $H\alpha$ (*centre*) and CO (*bottom*) velocity fields (models (A), (d) and (e) in Table 2). We remark on the larger radial extent of the CO data on the bottom plot. The contributions of the two best-fit Plummer components – modelling the galactic and circumnuclear disk – are shown in cyan and light green, and the sum of their contributions in purple. The red and blue curves correspond to the receding and approaching side of the velocity map. In Fig. A.1, we additionally show the $H\alpha$ rotation curve for model (e), where we enforce a more symmetrical curve. In the *middle panel*, the radial location of features A and B discussed in Sect. 6.1 is indicated.

a factor two the number of fitted spaxels, the output parameters are remarkably stable. The best-fit inclination $incl = 20.3 \pm 0.1^\circ$ is in excellent agreement with the one of 21° listed by Gadotti et al. (2019), the position angle $PA = 223.1 \pm 0.1^\circ$ is also very close to the one of 227° found by Sheth et al. (2010) and the systemic velocity $v_{\text{sys}} = 514.2 \text{ km s}^{-1}$ is only 6 km s^{-1} higher

than the one from LEDA (Paturel et al. 2003; Makarov et al. 2014). The best-fit centre is consistent – within uncertainties – with the $\text{Pa}\beta$ kinematic centre determined by Knapen et al. (2010) (see Fig. A.3). Given the large number of spaxel used in the fit, the statistical uncertainties derived on the fitted parameters are very low; in order to study the robustness of the fit in Appendix A we test three additional models against model (A), adopting different centres from literature values. Using the parameters found with model (A), we computed the rotation curve shown in the top panel of Fig. 4, on top of which we overplot the contribution of the two Plummer components. The agreement between both sides of the rotation curve is very good for $r \gtrsim 50 \text{ arcsec}$ (1.1 kpc). Within the first kpc, large discrepancies are observed, with the approaching side rotating faster than the receding one. Regardless of the chosen parameters, it is not possible to make the slopes on both sides of the galaxy coincide within the first 100 pc, indicating that the central stellar component is non-axisymmetric. The discrepancy at the very end of the rotation curve, on the other hand, is due to the decreasing S/N at the edge of the disk.

3.4.2. Analysis of the ionised gas velocity field

We fitted the observed $H\alpha$ velocity field with the same theoretical velocity distribution as for the stars. We tested several models, whose parameters are also given in Table 2. The best-fit model is model (a). However, the $H\alpha$ velocity field is so perturbed that the hypothesis of an axisymmetric disk used by the model provides a χ_r^2 much higher than the one computed for the stellar disk, and does not allow to correctly determine the inclination of the galaxy, notoriously the most difficult parameter to fit (e.g., Epinat et al. 2008). The problem persisted even when masking the central region. To overcome this, we fitted a second model (model b) in which we fixed the inclination to the one of the stellar disk. This change only affected the χ_r^2 parameter (which increases by $<1\%$), clearly indicating that the inclination is relatively decoupled from the other parameters. The bottom row of Table 2 shows the average difference between the two sides of the rotation curve. In the literature, the systemic velocity is often determined by fitting a one-dimensional rotation curve. In this case, the amplitude of each side of the curve is matched by adjusting the centre location. On the other hand, when fitting a two-dimensional velocity field as in this work, if the receding and approaching sides display an asymmetric LoS velocity distribution, a difference in rotational velocity (ΔV_{rot}) may appear between the two sides of the rotation curve. We therefore fitted a third model (model c), where we additionally fixed $\Delta V_{\text{rot}} = 0$, in order to make the rotation curve more symmetric. This resulted in a moderate increase in χ_r^2 (5%). Finally, we produced two more models (models d and e) in which we fixed the centre of rotation to the one determined from the stellar disk. This was motivated by the fact that the potential well of the galaxy is dominated by the mass of the stars and of the dark matter halo. In addition, this will facilitate the comparison between the stellar and the gaseous disks. With respect to model (d), in model (e), we also fixed $\Delta V_{\text{rot}} = 0$. The only parameter marginally affected was the systemic velocity (v_{sys}). We show the rotation curve corresponding to model (d) in Fig. 4 (middle panel). In the figure, we also indicate the radial location of the central kinematic features that will be discussed in Sect. 6.1 (A and B, black arrows). In Fig. A.1, we include the $H\alpha$ velocity rotation curve produced with model (e) as a comparison.

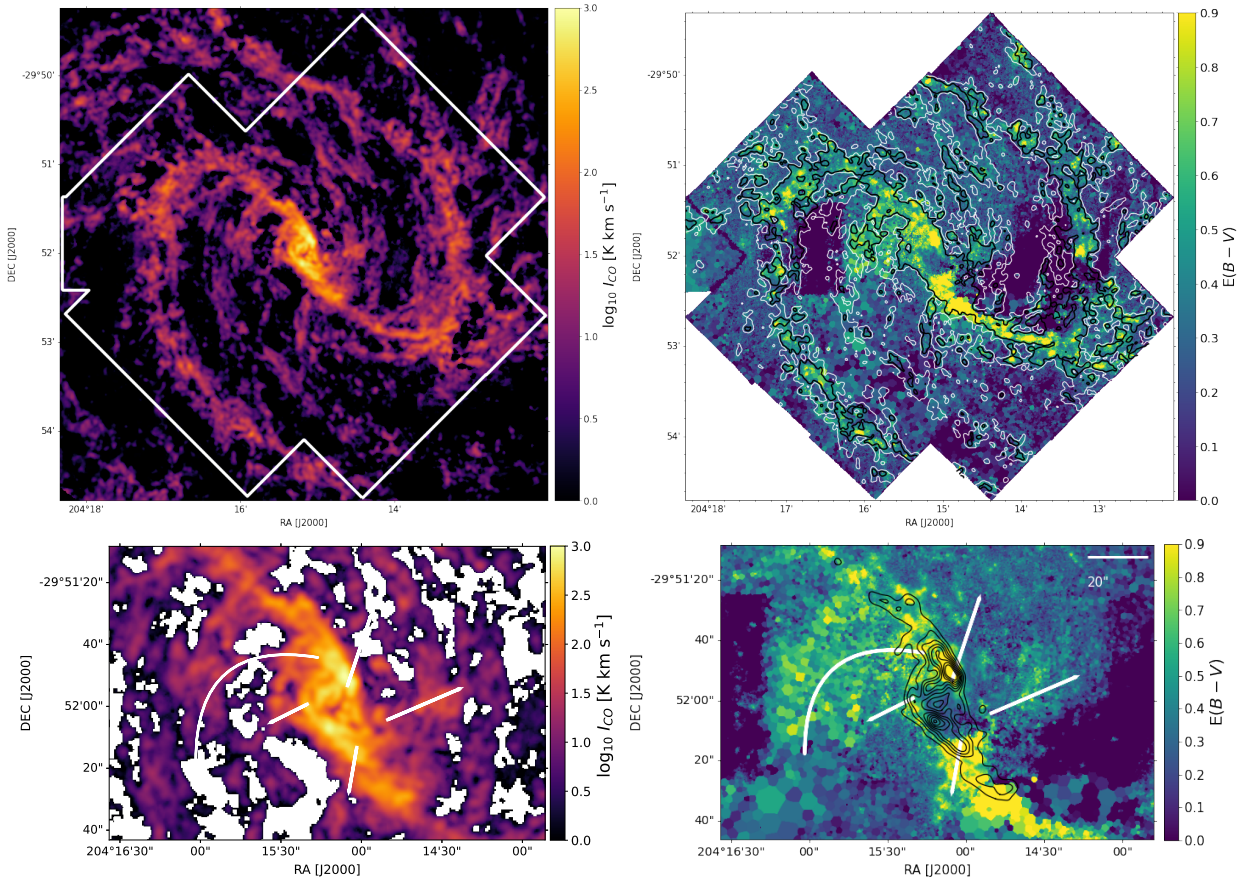


Fig. 5. Extinction traced by the ALMA and MUSE data. *Left panels:* CO(2-1) molecular gas emission from ALMA. *Right panels:* extinction map derived from the MUSE $H\beta/H\alpha$ ratio. *Bottom panels:* zoom-in into the central region, where the white lines mark the position of the features discussed in Sect. 6. The contours in the *top right panel* indicate CO(2-1) emission at 5 (white) and 15 (black) $K km s^{-1}$ (corresponding to $\Sigma_{mol} \sim 30$ and $100 M_{\odot} pc^{-2}$); the black contours in the *bottom right panel* range from 90 to $800 K km s^{-1}$ in steps of ~ 90 (corresponding to $\Sigma_{mol} \sim 600\text{--}5350 M_{\odot} pc^{-2}$).

3.4.3. Analysis of the CO gas velocity field

Finally, we fitted the CO data (‘mom1 with prior’ map⁸, see Leroy et al. 2021b) with the same two Plummer profiles, obtaining the best fit model (α) in Table 2. However, the best fit model exhibits a large inclination $incl = 35^{\circ}$, which is interestingly very close to the one derived from the best-fit $H\alpha$ model (37.9°); this indicates that the warm and cold gas kinematics are similar. For the same reasons mentioned above, in model (β), we fixed the inclination of the CO component to the one of the stellar disk, leaving the other parameters free. None of the fitted parameters were affected by this; only the χ_r^2 increases by $<2\%$. For model (γ), we also fixed the centre of rotation of the CO disk to that of the stars. This increased the χ_r^2 by a further $\sim 7\%$ with respect to model (β). To facilitate the comparison with the stellar and ionised gas component, in Fig. 4 (bottom panel) we show the rotation curve obtained from model (γ). We remark that since the area spanned by the ALMA data is much more extended than that of MUSE, the CO rotation curve extends $\sim 50\%$ farther. The first kpc is as difficult to fit as for the $H\alpha$ component, but we observe a fairly good agreement between the warm and the cold gaseous component. The receding side of both components shows a larger velocity up to the end of the MUSE rotation curve. Beyond this radius, the CO rotation curve indicates that

the receding side velocities are lower than the approaching side ones.

4. Extinction traced by the molecular and ionised gas

We estimated the extinction from the $H\beta/H\alpha$ ratio with PYNEB (Luridiana et al. 2015). We assumed an intrinsic ratio $H\alpha/H\beta = 2.863$ (corresponding to case B recombination with $T_e = 10^4 K$ and $n_e = 100 cm^{-3}$, Osterbrock & Ferland 2006) and a Cardelli et al. (1989) extinction law. The $H\beta/H\alpha$ ratio map was obtained by spatially binning the gas cube to a $S/N \simeq 20$ in $H\beta$ with the Voronoi tessellation technique. The lines were fitted with a single component Gaussian profile, as described in Sect. 3.2.

The resulting extinction map is shown in Fig. 5 (right panels). Because dust and gas are usually well mixed (e.g., Bohlin et al. 1978), we expect extinction and emission from gas to trace one another, modulo complications due to geometry and the presence of foreground and background sources, as observed for example with CALIFA by Barrera-Ballesteros et al. (2020). By comparing the extinction map with the CO intensity emission traced by ALMA (left panels in Fig. 5), we observe that indeed regions with high extinction correspond to dense molecular gas, with a surface density larger than $100 M_{\odot} pc^{-2}$ (black contours in the top right panel Fig. 5). This is particularly

⁸ This map uses a high completeness, in order to cover the larger possible number of sightlines.

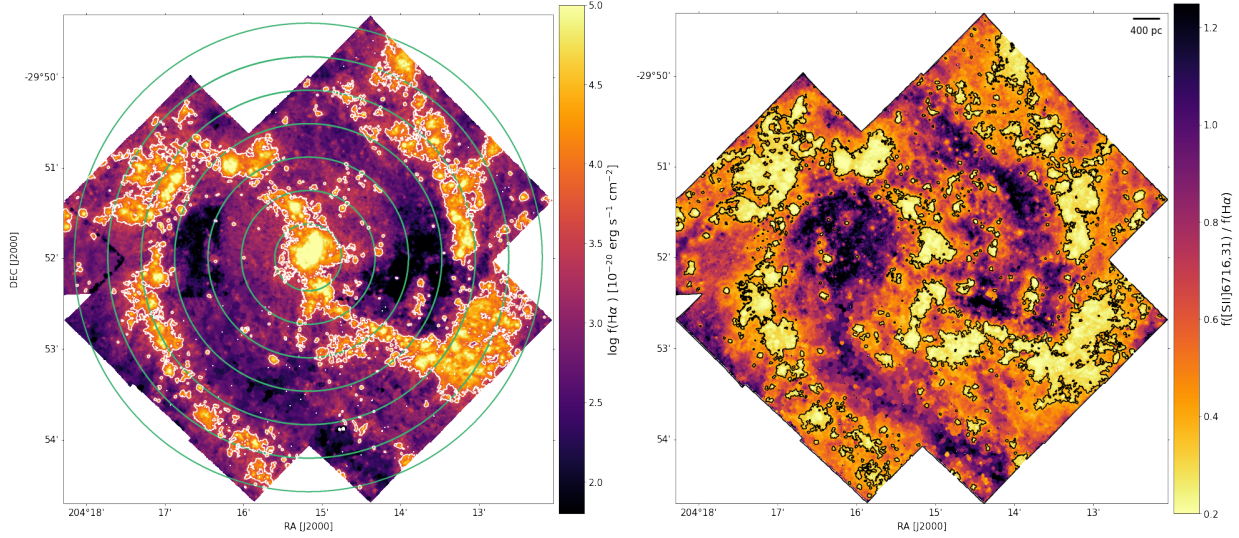


Fig. 6. Maps of $H\alpha$ (left panel) and $[S\ II] \lambda 6716,31/H\alpha$ (right panel) emission. Both maps have been corrected for extinction and deprojected. The contours indicate the outer limit of star-forming regions and correspond, respectively, to a cut in $SB_{H\alpha} = 1.23 \times 10^{-15} \text{ erg s}^{-1} \text{ cm}^{-2} \text{ arcsec}^{-2}$ and $[S\ II]/H\alpha = 0.29$. In green we indicate the annular sectors for which we compute the radial trends in Fig. 7.

evident along the spiral arms, where the extinction is clearly higher ($E(B - V) \gtrsim 0.5$) with respect to interarm region, due to the presence of dense gas. In the bottom right panel of Fig. 5, we show a zoom-in of the central region with CO emission overlaid in black on the extinction map. We observe two high density peaks in the molecular gas density distribution. These regions spatially coincide with the circumnuclear ring and dust inner bar reported in Elmegreen et al. (1998), and also studied by Callanan et al. (2021) in dense gas tracers. The northern peak in CO coincides with the approaching part of the circumnuclear disk observed in Sect. 3.1, and with a peak in the gas extinction map. The southern CO peak (receding part of the circumnuclear disk) shows very low extinction values. Given the inclination of the galaxy, we interpret this as a perspective effect on the vertical separation of the gas, due to the denser molecular gas residing deeper in the disk: the low extinction traced by the ionised gas would then be estimated based on line ratios from gas that is on top of the CO layer.

5. Properties of the ionised gas

5.1. $H\ II$ region identification and fraction of DIG

In Fig. 6 (left panel), we show a map of the intensity of the $H\alpha$ line, obtained by fitting the line in the gas cube spatially binned to a $S/N \approx 20$ in $H\alpha$. We separated the $H\alpha$ emission into $H\ II$ regions and DIG using the Python package ASTRODENDRO⁹. We remark that within the scope of this work we only require the outer boundaries of star-forming complexes. The detection of individual $H\ II$ regions will be presented in an upcoming work (Della Bruna et al., in prep.). The data were organised into a hierarchical tree structure of a given depth and minimum leaf size. We set the minimum size of the leaves based on the typical PSF measured at $H\alpha$ ($FWHM = 4.3 \text{ pixels} \equiv 0''.86$) and we fixed the optional `min_delta` parameter (minimum difference in flux between two separate structures) to zero. We set the depth of the tree to a surface brightness (SB) threshold corresponding to an $H\ II$ region ionised by a single low-luminosity O star. We determined this low luminosity threshold using the models of

⁹ <https://dendrograms.readthedocs.io>.

Martins et al. (2005) (Table 1 in their work), which predict an ionising photon flux $\log Q(H^0) = 47.56 \text{ photons s}^{-1}$ for a O9.5 class V star. In the case B approximation¹⁰, the $H\alpha$ luminosity is related to the ionising photon flux as

$$L(H\alpha) [\text{erg s}^{-1}] = \frac{\alpha_{H\alpha}^{\text{eff}}}{\alpha_B} h\nu_{H\alpha} \cdot Q(H^0) [\text{s}^{-1}],$$

where $\alpha_{H\alpha}^{\text{eff}}$ is the effective recombination coefficient at $H\alpha$ and α_B is the case B recombination coefficient. Assuming an electron temperature and density $T_e \sim 10\,000 \text{ K}$ and $n_e = 10^3 \text{ cm}^{-3}$, this gives (Draine 2011):

$$L(H\alpha) = 1.37 \times 10^{-12} Q(H^0).$$

We obtained thus $L(H\alpha) = 4.97 \times 10^{35} \text{ erg s}^{-1}$, corresponding to a SB threshold of $1.23 \times 10^{-15} \text{ erg s}^{-1} \text{ cm}^{-2} \text{ arcsec}^{-2}$, where we assumed an $H\ II$ region diameter of 10 pc (lower limit estimate). We note that our SB cut is slightly deeper than the one applied in the recent work by Poetrodjojo et al. (2019), which used a cut-off of $1.86 \times 10^{-15} \text{ erg s}^{-1} \text{ cm}^{-2} \text{ arcsec}^{-2}$ for their $H\ II$ regions sample. The outer contours of the resulting tree are shown in white in Fig. 6 (left panel). By inverting the $H\ II$ mask obtained from the dendrogram, we found an (extinction corrected) DIG fraction $f_{\text{DIG}} = F(H\alpha)_{\text{DIG}}/F(H\alpha)_{\text{TOT}} \sim 13\%$. In order to get a first order correction for DIG contamination, we obtained the distribution of the $H\alpha$ emission over the entire FoV, and estimated its median value via sigma clipping. We then subtracted this value from the $H\ II$ regions emission. Correcting for the diffuse emission coincident with $H\ II$ regions results in a negligible increase of $\lesssim 0.1\%$.

We also estimated the fraction of DIG based on a cut in $[S\ II]/H\alpha$, as recently done by Kreckel et al. (2016) and Poetrodjojo et al. (2019). The advantage of this ratio over a simple cut in $H\alpha$ SB is that it is sensitive to the ionisation state of the gas, as shown in Fig. 6 (right panel): a high ratio (in black) traces regions where the ionising photons have $I_{S^+} = 10.4 \text{ eV} < h\nu < 13.6 \text{ eV} = I_{H^+}$, where I denotes the ionisation potential. An intermediate ratio (orange to purple) indicates gas with

¹⁰ Case B recombination assumes that photons emitted during recombination are immediately reabsorbed, so that recombinations directly to $n = 1$ are ignored.

$I_{H^+} = 13.6\text{ eV} < h\nu < 23.3\text{ eV} = I_{S^{++}}$ and a low ratio (yellow to orange) marks regions where sulfur is largely doubly ionised ($h\nu > 23.3\text{ eV}$). As remarked by Kreckel et al. (2016), a cut in $[S\text{ II}]/H\alpha$ is better to detect fainter regions, but the generally lower S/N of the $[S\text{ II}]$ lines can result in irregular boundaries. Figure 6 (right panel) shows a map of the $[S\text{ II}] \lambda 6716,31/H\alpha$ ratio, obtained by fitting the emission lines in the gas cube tessellated to $S/N \approx 20$ in the $[S\text{ II}] \lambda 6731$ line. We observe that the ratio is enhanced in the interarm regions, consistent with DIG observations in the Milky Way and in nearby galaxies (Madsen et al. 2006; Haffner et al. 2009). If the DIG is solely ionised by radiation leaking from H II regions, the enhanced ratios can be explained with the fact that photons escaping from density bounded regions have a harder spectrum between the H I and He I ionisation energies, due to partial absorption, and a softer spectrum at shorter wavelengths, as has been shown for instance by the simulations of a stratified ISM from Wood & Mathis (2004). In their work, Poetrodjojo et al. (2019) applied a cut $[S\text{ II}] \lambda 6716,31/H\alpha = 0.29$, based on typical ratios observed in H II regions and DIG in the MW (Madsen et al. 2006). We adopted the same limit, which results in the contours shown in Fig. 6 (right panel). We observe that the regions contours are similar but somewhat more conservative than the one selected from the $H\alpha$ map. We recovered a (reddening corrected) $f_{\text{DIG}} \sim 20\%$; also in this case correcting for the diffuse emission coincident with H II regions has a negligible impact ($\leq 0.01\%$). The recovered value is somewhat lower than the value of 30% estimated by Poetrodjojo et al. (2019) in M83 in the radial range $R \leq 2R_e$ (using the distance and R_e adopted in this work). The discrepancy could be due to the more accurate fitting of the stellar continuum in the MUSE data or to the difference in spatial coverage, depth and spatial and spectral resolution of the two datasets. For the remainder of this work, we adopt the H II region contours selected on the $H\alpha$ map as a reference.

In Fig. 7, we show the radial flux profile for the H II regions and the DIG. The profile was obtained by radially binning the reddening corrected and de-projected $H\alpha$ map in annular sectors of width $dr = 0.15 R_e$ (indicated in green in Fig. 6, left panel), and matching it with the H II regions contours. The DIG flux was corrected for the diffuse background emission as described above. The first point refers to the emission in the starburst region, $0 \leq R \leq 0.15 R_e$. We see that the luminosity of the H II regions is highest in the centre, due to the starburst activity, and then reflects the configuration of the spiral arms. The SB of the DIG follows a similar trend, although the minimum is offset by $0.15 R_e$. The resulting f_{DIG} ratio is shown in black in Fig. 7; we see that the DIG contribution to the total luminosity varies between 0.8% and 46%, peaking in the interarm region. The radial trends are in good agreement with what observed by Poetrodjojo et al. (2019, Fig. 6 in their work)¹¹.

5.2. BPT diagram analysis

We studied the physical conditions of the ionised gas in ‘BPT’ emission line diagrams (Baldwin et al. 1981; Veilleux & Osterbrock 1987). This set of diagrams offers a powerful tool to interpret ionised gas emission, as the location in the diagram is sensitive to parameters such as the electron density, metallicity, strength and hardness of the radiation field (see e.g., the review by Kewley et al. 2019). We inspected the full set of dia-

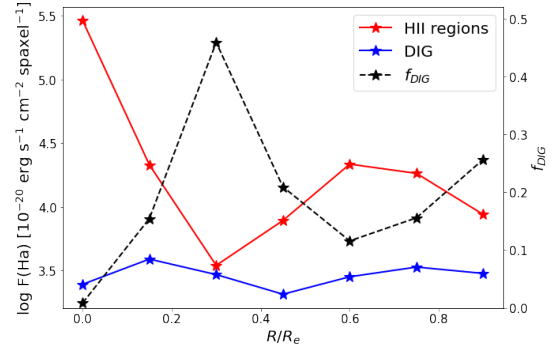


Fig. 7. $H\alpha$ normalised flux as function of radius for the H II regions (red) and DIG (blue), and resulting DIG fraction (black). The data are radially binned in annuli of width $dr = 0.15 R_e$ (shown in Fig. 6), and the flux has been normalised by the number of spaxels in each annulus. The H II regions flux has been corrected for diffuse emission.

grams, showcasing $[N\text{ II}]/H\alpha$, $[S\text{ II}]/H\alpha$ and $[O\text{ I}]/H\alpha$ as function of $[O\text{ III}]/H\beta$. In each diagram the fluxes were obtained by single component Gaussian fitting of the emission lines in the gas cube tessellated to a $S/N = 20$ in the weakest line of interest ($[O\text{ III}] \lambda 5007$ for the N2- and S2-BPT diagrams, and $[O\text{ I}] \lambda 6300$ for the O1 diagram). Typical Voronoi bin sizes in the H II regions vs. the DIG are: $0''.3$ vs. $0''.9$ in the O III binning and $0''.7$ vs. $2''$ in the O I binning. We caution that bins located in H II regions are typically below the seeing limit, especially in the blue end of the spectrum (where PSF sizes range between 0.7–0.9 arcsec). However, this should not have a relevant impact within the scope of this work.

The resulting diagrams are shown in Fig. 8: each point corresponds to a Voronoi bin, and is colour-coded as located in an H II region (purple) or in the DIG (green). The black dashed line indicates the location of the ‘extreme starburst’ line by Kewley et al. (2001), corresponding to the upper limit for gas excited purely by SF. Emission above this limit likely originates from shocks or active galactic nuclei (AGN) activity. In Fig. 9 (top panel) we show again the N2-BPT diagram, with each point colour-coded according to its orthogonal distance from the extreme starburst line ($\Delta N\text{ II}$). $\Delta N\text{ II}$ increases from the bottom left (dark blue, purely SF gas) towards the top right corner (orange-red, purely ionised by shocks or AGN) of the diagram. In the figure, we additionally show the empirical line of Kauffmann et al. (2003, black dotted line), denoting a more stringent limit for gas excited by pure photoionisation. Points located between this line and the extreme starburst line (yellow-green) are likely excited by a mix of SF and shocks or AGN. In the bottom panel of Fig. 9 we show the corresponding ‘2D-BPT’ diagram, where each spatial bin is colour-coded according to $\Delta N\text{ II}$. We observe that the spiral arms regions stand out as purely SF, the diffuse gas immediately surrounding the regions shows a composite emission, and some of the interarm regions – especially at $0.2\text{--}0.4 R_e$ – show a clear signature of shocks.

Finally, we assessed the overall fraction of $H\alpha$ luminosity originating from SF (regions with $\Delta N\text{ II} \leq 0$) and shocks ($\Delta N\text{ II} > 0$). We observe that, as expected, in H II regions SF accounts for most of the $H\alpha$ flux (99.8% of the flux originates from regions where photoionisation is the dominant mechanism), whereas bins classified as DIG have a mixed contribution from both photoionisation-dominated regions (accounting for 94.9% of the flux) and shock-dominated regions (accounting for the remaining 5.1%).

¹¹ We note that using the distance and R_e adopted in Poetrodjojo et al. (2019), the MUSE data presented in this work only span the range $R \leq 0.8 R_e$ in their Fig. 6.

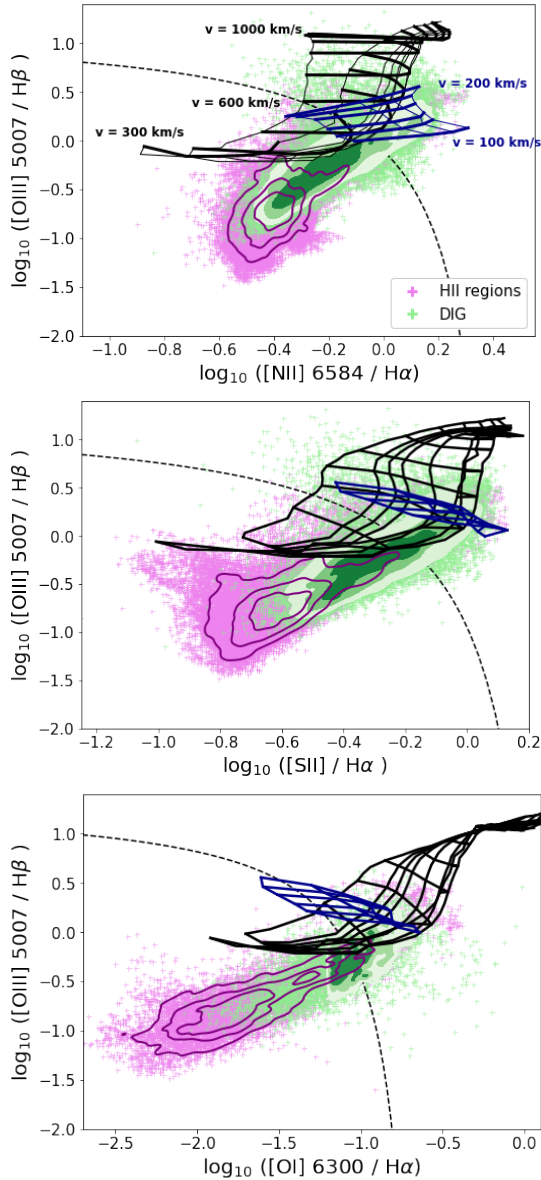


Fig. 8. BPT emission line diagrams. Each point corresponds to a Voronoi bin, and is colour-coded as located in an H II region (pink) or in the DIG (green). The contours overplotted on the data correspond to iso-proportions of the density, with a probability mass $\leq 0.25, 0.5, 0.75$ and 1 . The data are compared to the extreme starburst line from Kewley et al. (2001, black dashed line), the fast shock models from Allen et al. (2008, black grid), and slow shock models from Rich et al. (2011, blue grid).

We compared our observations with models of fast and slow shocks (black and blue grid in Figs. 8 and 9). The black grid corresponds to the fast shock models of Allen et al. (2008). We use the models that include the photoionising shock precursor, with metallicity $Z = 2 Z_{\odot}$ and electron density $n_e = 1 \text{ cm}^{-3}$. We show the model grid spanning $b = (0.001-100) \mu\text{G}$ in magnetic field strength and $v_s = 290-1000 \text{ km s}^{-1}$ in shock velocity. The blue grid displays the slow shock models described in Farage et al. (2010) and Rich et al. (2011). These models describe shocks driven into the galactic disk by ram pressure originating as a cloud of cool gas (possibly a filament from a merger remnant) falls into the hot ISM halo of a galaxy. The full model grid covers the range $12 + \log(\text{O}/\text{H}) = 7.39-9.39$ ($\sim 0.05-5 Z_{\odot}$) in metallic-

ity and $v_s = 100-200 \text{ km s}^{-1}$ in shock velocity; we show however only the super-solar range, $Z \geq 8.69$. We observe that the points located beyond the SF limit overlap with shock model grids. In particular in the [N II] diagram, we observe a cloud of points with $\log[\text{N II}]/\text{H}\alpha > 0$ that only overlaps with the slow shock models: we investigate more closely these regions in Sect. 6, where we study the kinematics and ionisation state of the starburst region.

6. Analysis of the starburst region

We now analyse in more detail the kinematics and ionisation state of the starburst region, indicated by a black rectangle in Fig. 2 (left panel) and shown in more detail in Fig. 10. In the figure, we outline the approximate location of the outer dust ring (of radius $\approx 9''$) and inner bar as determined by Elmegreen et al. (1998) (purple lines) and mark the kinematic features that will be discussed in the rest of this section (black lines).

6.1. Kinematics of the central starburst region

In Fig. 11 we show a close up view of the kinematics of the central region. In Fig. 12 we additionally inspect the ionised gas kinematics obtained from the 2-component Gaussian analysis. Grey shaded areas in the maps of the second component indicate regions in which the line was best fit by a single component (see description of the fitting method in Sect. 3.2).

In the stellar kinematics (top panels in Fig. 11) we observe a fast rotating nuclear component ($\sim 30'' \approx 700 \text{ pc}$ in diameter), already reported by Gadotti et al. (2020). We stress that the alignment of the rotation axis of this inner component (black dashed line) and the stellar bar is purely coincidental, and is expected to significantly vary over secular timescales. We also observe a dip in velocity dispersion ($\sigma < 60 \text{ km s}^{-1}$) at the location of the starburst arc and along the dust lane west of the arc. Similar ‘central dispersion drops’ were reported by Emsellem et al. (2001) and Emsellem (2004) as being possibly due to a dynamically cold stellar component that has formed as a consequence of a bar-driven gas accretion episode.

The ionised gas kinematics are – as already observed in Sect. 3 – more complex. In the velocity map of the single component fit (centre left in Fig. 11) and in the first component of the double Gaussian fit (top left in Fig. 12), we observe a similar signature of a rotating circumnuclear disk, as already traced by the stellar kinematics. On the east of the nucleus, we observe a stream of gas (labelled as feature C), extending for $50''$ ($\approx 1250 \text{ pc}$) and having a velocity difference $\Delta v \approx +30 \text{ km s}^{-1}$ with respect to the surrounding disk rotation. The stream is surrounded by an extended region ($\sim 1000 \times 1600 \text{ pc}$) having an enhanced velocity dispersion $\approx 60-80 \text{ km s}^{-1}$. This feature was already reported in molecular gas by Lundgren et al. (2004) and in ionised gas by Fathi et al. (2008) as a potential inflowing stream of gas into the central starburst. Also Piqueras López et al. (2012) observe a global velocity gradient in the central region that is pointing to the possible presence of an inflow.

Surrounding the nucleus in the map of the second velocity component (second row on the left in Fig. 12), we also observe two conical features on each side of the stellar bar (labelled as features A and B). The two cones are $20'' \approx 500 \text{ pc}$ in size, have a $\Delta v \approx \pm 100 \text{ km s}^{-1}$ on top of the disk rotation and a high velocity dispersion $\sigma_{\text{comp2}} \geq 80 \text{ km s}^{-1}$ (second row on the right in Fig. 12). Cone A appears blueshifted along our LoS, while cone B appears redshifted. In Fig. 5 (bottom panels), we also observed that at the location of cone A there is a peak in the molecular gas emission, whereas the ionised gas traces low extinction. We

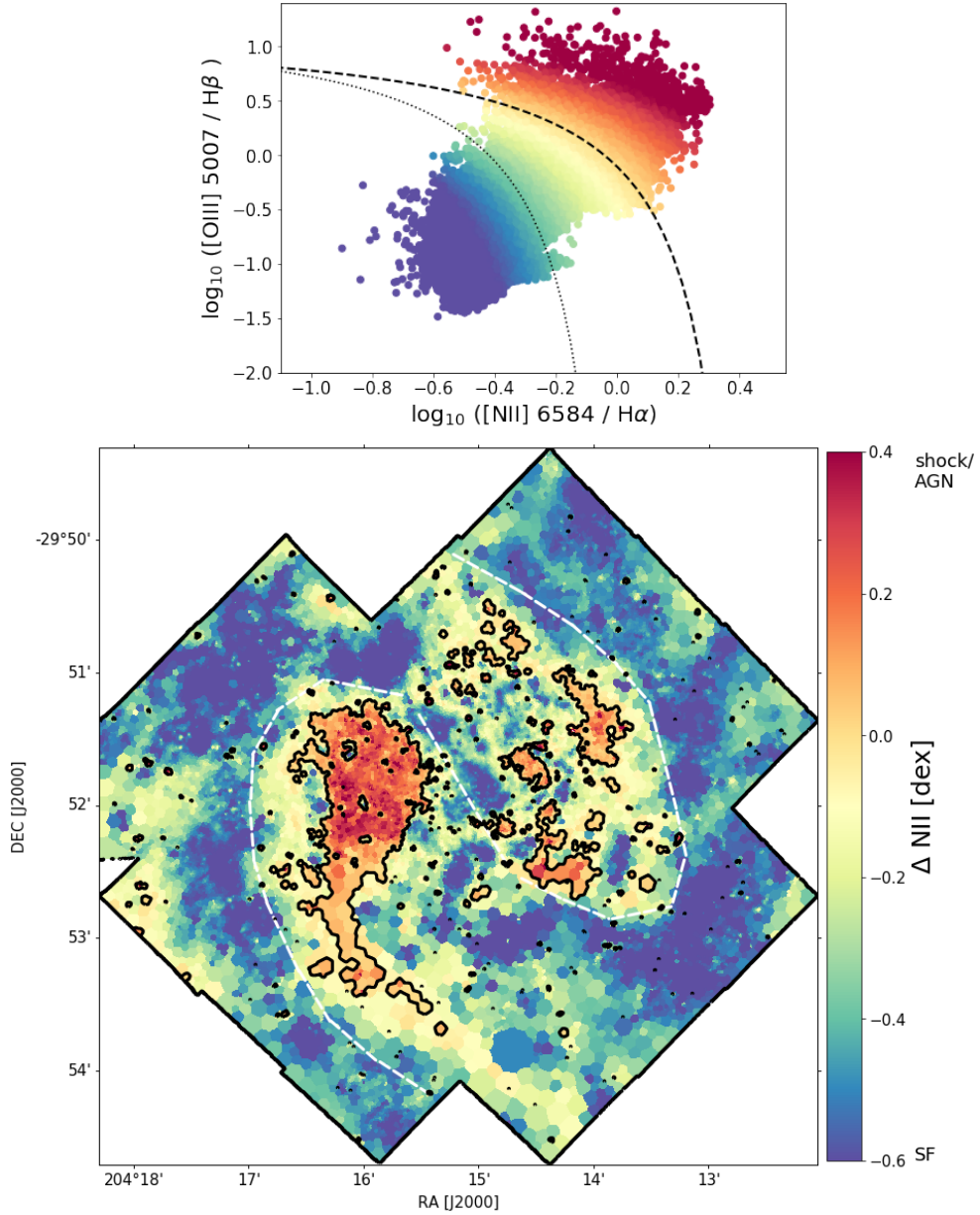


Fig. 9. 1D (*top panel*) and 2D (*bottom panel*) N II-BPT diagram, with each point colour coded according to its distance from the extreme starburst line of Kewley et al. (2001, black dashed line in the top panel). The distance ($\Delta \text{N II}$), ranges from dark blue for pure SF to red for pure shock or AGN emission. In the *top panel*, we also show the empirical demarcation line from Kauffmann et al. (2003, black dotted line), indicating a more stringent limit for photoionised gas. In the *bottom panel*, the black contours correspond to $\Delta \text{N II} = 0$ and white dashed lines indicate the position of the bar and spiral arms.

interpreted this as the fact that the CO emitting gas is located ‘behind’ the ionised gas along our LoS; together with the fact that cone A appears blueshifted, this could indicate that the gas is moving towards us. On the other hand, we do not see a mismatch between CO and $E(B - V)$ along cone B, which might indicate that the ionised gas is moving away from us. Features A and B also clearly stand out in the $\text{H}\alpha$ rotation curve¹², as remarked in Fig. 4 (black arrows). On the third and fourth row of Fig. 12, we show the velocity difference between the two Gaussian components, as well as three example spectra, corresponding to features A, B and C. We observe that at the centre of the two cones, the

velocity difference between first and second component reaches 200 km s^{-1} .

In the molecular gas (third row in Fig. 11) we observe again the signature of a circumnuclear disk. We also observe some clouds of redshifted molecular gas coincident with feature C. Along these lines of sight, we observe two or three distinct bright peaks of emission, as illustrated in Fig. 13. All but one of these components correspond to gas with a velocity compatible with the galactic rotation, whereas the remaining component is redshifted by $\sim 100 \text{ km s}^{-1}$ with respect to the disk CO emission. For these complex spectra, we remark that the corresponding mom1 velocity value corresponds to an average of the features. In fitting Gaussian models to some of these clouds, we find that the velocity dispersion of the CO emission at the velocity expected from the circular rotation field is $7\text{--}20 \text{ km s}^{-1}$, whereas

¹² Both on the receding side, due to their position with respect to the angular sector used to compute the curve.

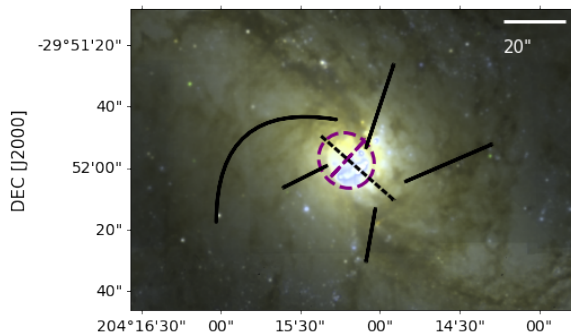


Fig. 10. Morphology of the M83 starburst region. The background image shows a zoom-in into the three colour stellar composite from MUSE (Fig. 2). The purple dashed lines indicate the schematic location of the outer circumnuclear ring and dust inner bar from Elmegreen et al. (1998). The brightest region of star formation (‘starburst arc’) is visible inside the ring. Black lines indicate the location of the kinematic features discussed in Sect. 6. The scalebar of $20''$ corresponds to ≈ 500 pc at the distance of our target.

the redshifted component has a larger velocity dispersion ≈ 25 km s $^{-1}$.

The peak brightness of the redshifted CO gas blobs is 0.3 to 0.5 K, their velocity dispersions are 15–25 km s $^{-1}$, and their clouds are marginally resolved by the ALMA beam (diameters $\gtrsim 50$ pc). Using our adopted conversion factors, the redshifted blobs would have equivalent surface densities of 70–200 M_{\odot} pc $^{-2}$ and a total mass of $4 \times 10^6 M_{\odot}$. At these surface densities and velocity dispersions, such gas would be typical of what is found in the central regions of barred galaxies¹³ (e.g., Sun et al. 2020). We remark that features A and B, on the other hand, do not stand out in the CO map. In the remainder of this section, we study features A, B and C in more detail, and in Sect. 7 we discuss their possible origin.

6.2. BPT analysis of the starburst region

In Fig. 14 we show a close up view of the 2D N II-BPT diagram presented in Fig. 9. Blue shaded regions in the map correspond to areas whose emission is overlapping purely with slow shock models (area spanned exclusively by the blue grid in the top panel of Fig. 8). We observe that most of the region surrounding stream C, as well as the far end of cone B (at $d \geq 20''$ from the galactic centre) are consistent with pure slow shocks.

We also performed a BPT analysis analogous to Sect. 5.2 for the two Gaussian components separately. We fitted the relevant emission lines in the cube binned to a $S/N \approx 20$ in the [O III] $\lambda 5007$ line. Given that for weaker emission lines double components might be harder to disentangle, we first performed a fit to the $H\alpha$ line and then fixed the kinematic parameters obtained from this fit for all emission lines.

¹³ We estimate however that these clouds are likely not self-gravitating – if our assumed α_{CO} value is correct – by evaluating the ratio of the kinetic energy (K) to the gravitational binding energy (U_{grav}) under a simple spherical model (e.g., Sun et al. 2020; Rosolowsky et al. 2021) along a single line of sight with a radius of half the beam size ($R = 25$ pc), $\sigma_{CO} = 15$ km s $^{-1}$ and a surface density of $100 M_{\odot}$ pc $^{-2}$. The total mass in a synthesised beam is then $2 \times 10^5 M_{\odot}$ and $K \sim 30 U_{grav}$. Alternatively, their opacity and corresponding conversion factors may be lower than for disk clouds, as observed in some galaxy centres (Sandstrom et al. 2013).

In the top panels of Fig. 15 we show the resulting N2-BPT diagrams. Hereby, points with an uncertainty on either [N II]/ $H\alpha$ or [O III]/ $H\beta$ greater than 50% of the ratio are masked, in order to remove bad fits. We observe that both components are tracing both SF and shocks, although the second component extends to more extreme values of [N II]/ $H\alpha$. This is more clearly visible in the 2D-BPT diagram shown in the bottom panels of Fig. 15. We see that cones A and B are – in both components – consistent with star formation near the stellar bar, and only become shocked at a projected distance $d \geq 20''$ from the galactic centre, perhaps tracing an outflow originating from the starburst region that is shocking into the surrounding gas. We discuss this further in Sect. 7.

6.3. Shock-sensitive emission line ratios

The top two panels of Fig. 16 show a map of the [O III] $\lambda 4959, 5007/H\alpha$ ratio for the central region (maps of the full FoV can be found in Appendix B). The maps were obtained by fitting the emission lines with a double Gaussian component in the gas cube spatially binned to a $S/N \approx 20$ in the [O III] $\lambda 5007$ line. A high [O III]/ $H\alpha$ ratio is indicative of gas with a high ionisation state, where emission from doubly ionised oxygen (tracing photons with $h\nu \geq 35.1$ eV) is non-negligible with respect to ionised hydrogen (e.g., Veilleux & Osterbrock 1987). We observe that both the region surrounding stream C and the far end of cone B (at $d \geq 20''$ from the galactic centre) have a high ratio both in the first ([O III]/ $H\alpha \approx 0.4$ – 0.8) and in the second Gaussian component ([O III]/ $H\alpha \approx 0.5$ – 1.1). Cone A, on the other hand, only shows a very locally enhanced ratio ([O III]/ $H\alpha \approx 1$) in the second component. This could however in part be due to the extremely high extinction at this location, as traced both by the ionised and molecular gas (bottom panel of Fig. 5).

In the bottom panel of Fig. 16 we show a map of the [O I] $\lambda 6300/H\alpha$ ratio, obtained from a single Gaussian component; we do not perform a 2-component fit to the [O I] line due to its weak nature. A high ratio of [O I] emission with respect to $H\alpha$ is indicative of the presence of shocks (Veilleux & Osterbrock 1987). We observe that also in this map both the region surrounding stream C and the far end of cone B have an enhanced ratio ([O I]/ $H\alpha \approx 0.5$ – 0.7).

7. Discussion

7.1. Kinematic features in the starburst region

Both models and observations have shown how bars in massive disk galaxies are responsible for physical processes that result in new stellar structures such as nuclear discs or rings and inner bars (Gadotti et al. 2020, and references therein). These processes are driven by bar-induced resonances resulting from the non-axisymmetric potential (e.g., Binney & Tremaine 1987), such as Lindblad resonances¹⁴. Dynamical models for the evolution of gas in barred spiral galaxies in 1D (Krumholz & Kruijssen 2015; Krumholz et al. 2017) and 2D (Simkin et al. 1980; Regan & Teuben 2003) are able to model the creation of a nuclear ring within the inner Lindblad resonance (ILR). The main processes involved are described in detail in

¹⁴ Lindblad resonances occur for $2(\Omega - \Omega_p) = \pm\kappa$, where κ is the frequency of the radial oscillation and Ω_p and Ω are, respectively, the angular velocity of the bar and of the stars/gas (neglecting the effect of spiral arms).

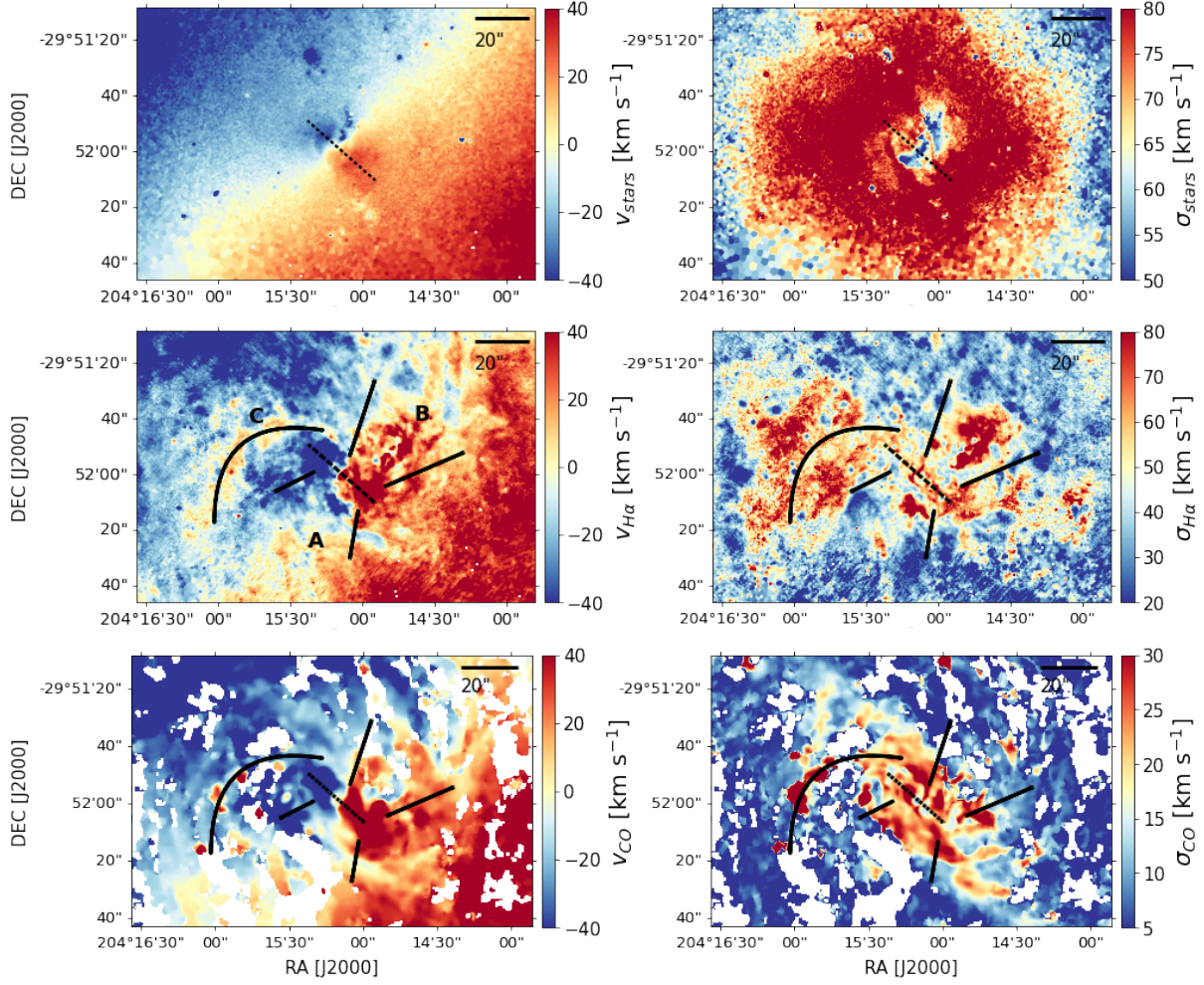


Fig. 11. Close up view of Fig. 3 showcasing the kinematics of the starburst region. All velocity maps (*left panels*) have been corrected for the systemic velocity; no inclination correction has been applied. Black lines mark the kinematic features discussed in Sect. 6.

Krumholz & Kruijssen (2015); see also Renaud et al. (2015); we briefly summarise them here.

In a first phase, the bar exerts torques on the orbiting material. As the gas loses angular momentum, it moves inwards and by energy conservation, the gravitational potential energy is transformed into turbulent energy, resulting in an increase in velocity dispersion. In a second phase, due to the increased velocity dispersion and the mostly flat rotation curve (low shear) within the ILR, acoustic instabilities develop in the gas. This allows for a more efficient transport of angular momentum, and leads to an inflow of gas with high turbulent pressure that is extremely gravitationally stable and has a low SFR. In a third phase, gas starts to build up on the stable ILR orbit, eventually leading in gravitational instabilities that cause fragmentation and collapse, resulting in a circumnuclear ring. The ring can form stars episodically (e.g., in the 1D dynamical models of Krumholz & Kruijssen 2015), or having an initially steady fuelling rate before fragmenting after ~ 10 Myr (e.g., in the hydrodynamical simulations from Emsellem et al. 2015).

In Sect. 6.1, we confirmed the presence of a circumnuclear disk, both in the stellar, ionised gas and molecular gas kinematics (Fig. 11). This feature had already been recently observed with MUSE (Gadotti et al. 2020), and has been postulated to coincide with an ILR. Recently, Callanan et al. (2021) analysed high resolution ALMA data mapping the central 500 pc at scales

of ~ 10 pc, and put forward a model in which the gas revolves around the centre in eccentric orbits. The study proved that the gas in the ring features strong azimuthal variations in velocity dispersion and intensity which are consistent with the expectations from 1D dynamical models (Krumholz & Kruijssen 2015; Krumholz et al. 2017). Furthermore, in their simple model scenario the starburst phase resulting from the disk instability is constrained to be highly localised, both in space and in time, resulting in very efficient stellar feedback.

We furthermore observed that both the ionised and molecular gas are tracing a flow of gas east of the nucleus (feature C in Fig. 11). Lundgren et al. (2004) were the first to report this feature in CO(2-1) and (1-0). Their observations traced – on top of a regular rotating disk – streaming motions along the spiral arms, with the strongest deviation on the NW side of the nucleus. This feature was later confirmed by Fathi et al. (2008) using Fabry-Perot data of the H α line across the disk. More recently, the Piqueras López et al. (2012) observed evidence of what they interpreted as a gas inflow also in high-resolution NIR IFS data mapping the central $\sim 200 \times 200$ pc. In our dataset, we observe that the stream has $\Delta v_{\text{H}\alpha} \simeq +30 \text{ km s}^{-1}$ with respect to the surrounding disk rotation (Fig. 11, centre left) and multiple peaks of emission at different velocities in the molecular gas (Fig. 13), one of which is redshifted by $\sim 100 \text{ km s}^{-1}$ with respect to the disk rotation and has an enhanced velocity dispersion

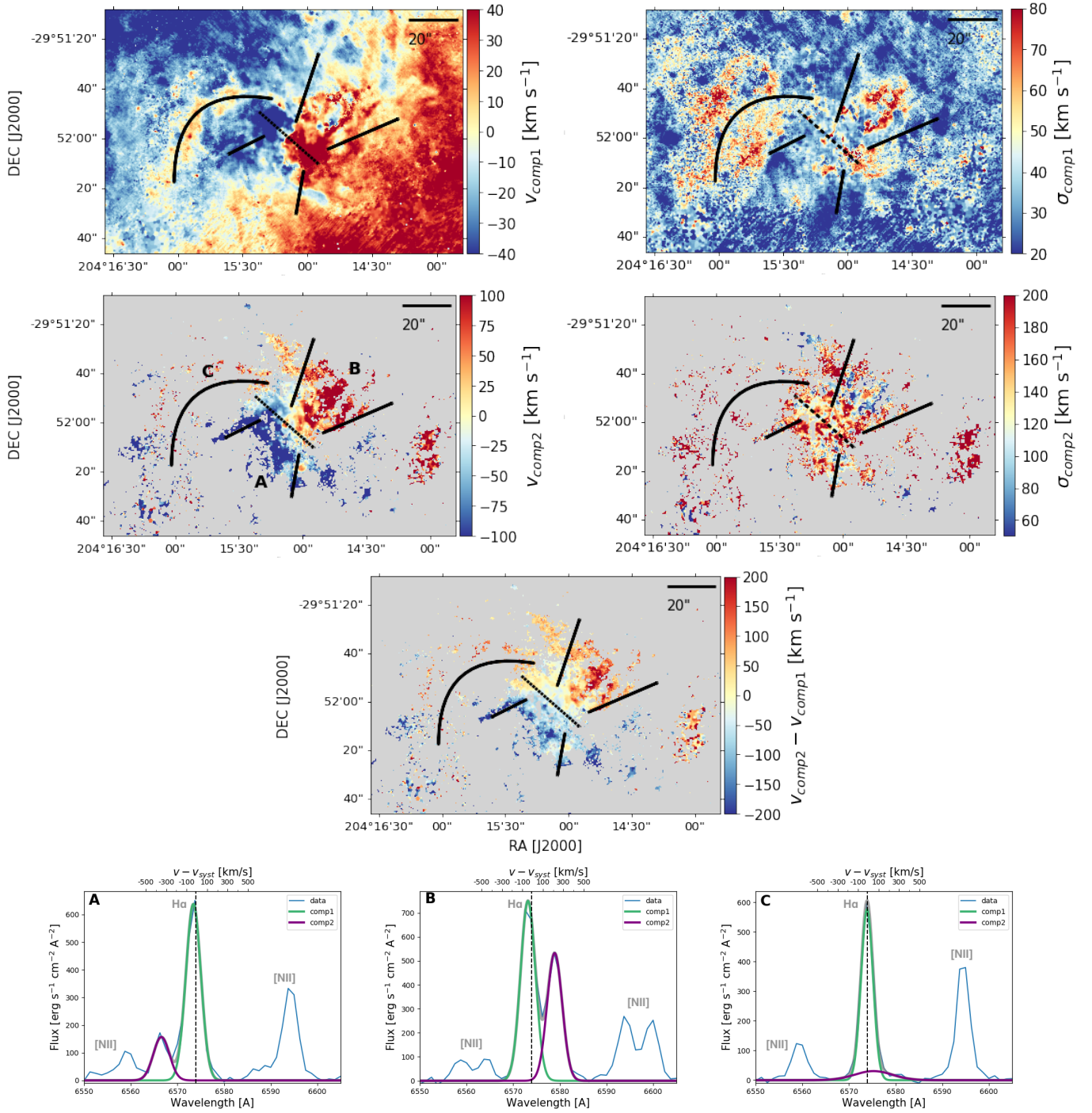


Fig. 12. Results from the 2-component Gaussian fit to the $H\alpha$ line. *First and second row:* $H\alpha$ velocity (*left panels*) and velocity dispersion (*right panels*) maps, of the two components. The velocity maps have been corrected for the systemic velocity; no inclination correction has been applied. The velocity dispersion has been corrected for instrumental effects. We draw attention on the different velocity and dispersion scales spanned by the first and second component. *Third row:* velocity difference between the two components (blue and red indicate, respectively, a second component that is more strongly blueshifted and redshifted with respect to the first one). Black lines mark the kinematic features discussed in Sect. 6. *Bottom row:* typical spectra of features A and B and C (see labels in the figure). In panels A and B, both the $H\alpha$ line and the $[N\text{II}]$ doublet are clearly doubly peaked, with $\Delta v \sim 300\text{ km s}^{-1}$. In panel C, both components are at similar velocity, but the second component has an extremely high $\sigma \sim 140\text{ km s}^{-1}$.

($\approx 25\text{ km s}^{-1}$). The MUSE data furthermore trace an extended region surrounding the stream ($\sim 1000 \times 1600\text{ pc}$) featuring: (1) a high velocity dispersion ($\approx 80\text{ km s}^{-1}$, Fig. 11, centre right); (2) $[N\text{II}]/H\alpha$ and $[O\text{III}]/H\beta$ ratios that situate the gas clearly above the line separating SF from shocks in a BPT diagram (Figs. 9 and 15), in a region consistent for most part with slow shock

models only (Fig. 14); (3) high ratios of $[O\text{III}]$ and $[O\text{I}]$ with respect to $H\alpha$ (Fig. 16), indicative of gas with a high ionisation state and of shocks; (4) the presence of bright molecular gas but weak $H\alpha$ emission (Fig. B.1).

We interpret feature C as the result of two main scenarios. A first possible physical picture is the superposition along

the LoS of the disk and an extraplanar layer of DIG. Boettcher et al. (2017) obtained a high-resolution ($\sigma_{\text{H}\alpha} = 23 \text{ km s}^{-1}$ vs. the MUSE resolution of 120 km s^{-1}) single slit spectrum cutting through feature C. Their data show the presence of two distinct Gaussian components: a narrow component tracing Galactic rotation and a broad component ($\sigma \approx 95 \text{ km s}^{-1}$) having a velocity lag of $\sim 25 \text{ km s}^{-1}$ (similar to what we observe in the MUSE data) and high ratios of $[\text{N II}]/\text{H}\alpha \sim 1.0$. The authors interpret this as the presence of an extraplanar layer of DIG, as broadly observed in other star-forming disks (see e.g., Rossa & Dettmar 2003; Lacerda et al. 2018; Levy et al. 2019; Rautio et al. 2022). This scenario is supported by the multiple peaks observed in the CO spectrum in Fig. 13.

In a second scenario, feature C could be a bar-driven inflow of gas located in the same plane as the disk; in this case the increased velocity dispersion would be tracing excess turbulence as the flow is shocked within the bar. An excess turbulence in the molecular gas could explain the lack of $\text{H}\alpha$ emission despite the bright CO emission along the stream, as the gas would be unable to collapse and form stars.

A final possibility could be a past interaction, possibly with the neighbouring galaxy NGC 5253 (1.8° in projected distance). This option has been taken into account by many authors in order to explain the peculiar morphology and kinematics of the central region, where the optical nucleus is offset from the kinematic centre (Thatte et al. 2000; Díaz et al. 2006; Mast et al. 2006; Houghton & Thatte 2008; Rodrigues et al. 2009; Knapen et al. 2010; Piqueras López et al. 2012) and the structure of the H I disk (Miller et al. 2009; Heald et al. 2016). However, given the extremely regular stellar rotation field and the general lack of global scale perturbances, we discard this hypothesis.

In the ionised gas kinematics resulting from the double component Gaussian fit (Fig. 12), we also observed two kinematic features (labelled as cones A and B) where the $\text{H}\alpha$ line is composed of two peaks, separated by a velocity $\Delta v \leq 200 \text{ km s}^{-1}$ (third and fourth row in Fig. 12) and a high velocity dispersion (up to 200 km s^{-1} , top and centre right in Fig. 12). The two cones appear, respectively, blue- and redshifted along our line of sight ($v \approx \pm 100 \text{ km s}^{-1}$). Cone B features at its far end ($d \geq 20''$ from the galactic centre): (1) $[\text{N II}]/\text{H}\alpha$ and $[\text{O III}]/\text{H}\beta$ ratios above the SF limit in a N2-BPT analysis (Figs. 9 and 15), in a region of the diagram that overlaps mostly with slow shock models (Fig. 14); (2) high ratios of $[\text{O III}]$ and $[\text{O I}]$ with respect to $\text{H}\alpha$ (Fig. 16), indicative of gas with a high ionisation state and/or shocks; (3) a relatively bright CO emission in a region with little SF (bottom left in Fig. 5 and left panel in Fig. 6). Cone A stands out less clearly in these tracers, perhaps owing to the high extinction at this location (see bottom right panel of Fig. 5). Nonetheless, we observe BPT line ratios indicative of shocks in the second Gaussian component (Fig. 15, for $d \geq 20''$) and a locally enhanced $[\text{O I}]/\text{H}\alpha$ ratio (central panel in Fig. 16).

So far, no AGN activity has been confirmed in M83, and hard X-ray observations (Yukita et al. 2016) constrain any AGN to be either highly obscured or to have an extremely low luminosity. Given the fact that the origin of cones A and B is offset from the galaxy's centre, the lack of shock-related emission immediately surrounding the central region and the presence of slow shocks, we favour over the presence of an AGN the hypothesis of a starburst-driven outflow cone shocking into the surrounding ISM. Similar starburst-driven bi-conical outflows have been observed in M82 (Shopbell & Bland-Hawthorn 1998; Leroy et al. 2015b), in which the outflow cones also feature a double component $\text{H}\alpha$ line with $\Delta v = 300 \text{ km s}^{-1}$, low $[\text{N II}]/\text{H}\alpha$ ratios compatible with photoionisation and an $[\text{O III}]/\text{H}\alpha$ ratio

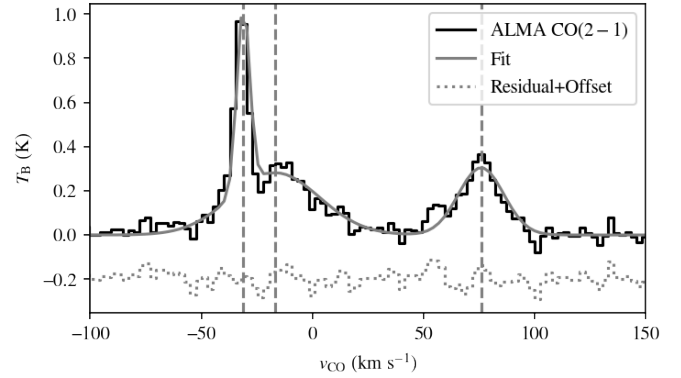


Fig. 13. ALMA CO(2-1) spectrum of one of the CO ‘blobs’ along feature C in Fig. 11 (one ALMA spaxel centred on RA = 204.266, Dec = -29.8665). The spectrum has been corrected for the systemic velocity. We observe three separate Gaussian velocity components. The component at $v_{\text{CO}} \sim -30 \text{ km s}^{-1}$ is associated with the spiral arm in the galaxy, and the component at -20 km s^{-1} traces broadening around the first one, likely associated with a bar orbit. We interpret the third component at $v_{\text{LSR}} \sim 80 \text{ km s}^{-1}$ as being associated with infalling material.

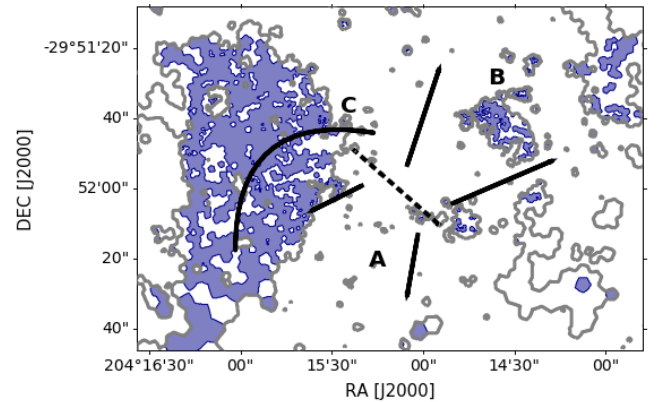


Fig. 14. Zoom-in into the 2D N II-BPT diagram from Fig. 9. The grey contours correspond to $\Delta \text{N II} = 0$. Blue shaded areas indicate regions whose emission is compatible with slow shock models only (blue grid in Fig. 8).

that increases along the outflow, as well as in NGC 253 (Bolatto et al. 2013) and ESO 338-IG04 (Bik et al. 2018). The scenario of a starburst- (rather than AGN-) driven outflow is also in better agreement with the low $[\text{S II}] \lambda 6716/6731$ line ratio observed throughout cones A and B (see e.g., Bik et al. 2018). The ratio is very close to the sensitivity limit ($[\text{S II}] \lambda 6716/6731 = 1.45$, corresponding to $n_e \leq 1 \text{ cm}^{-3}$, Draine 2011), and within the measurement errors is largely consistent with $n_e \leq 30 \text{ cm}^{-3}$. A starburst-driven outflow would be compatible with the scenario of a short-lived and localised starburst activity by Callanan et al. (2021), resulting in very efficient stellar feedback and, potentially, in nuclear outflows.

An alternative explanation could be the combination of past AGN activity followed by starburst emission. In this scenario, the AGN could have carved a path for the starburst feedback, and could explain the ‘jet-like’ morphology of the outflow and its extent.

Finally, what appear as redshifted and blueshifted cones along our line of sight could simply be the result of the superposition of bar-driven orbits, resulting from the non-axisymmetric and time varying potential. However, this effect

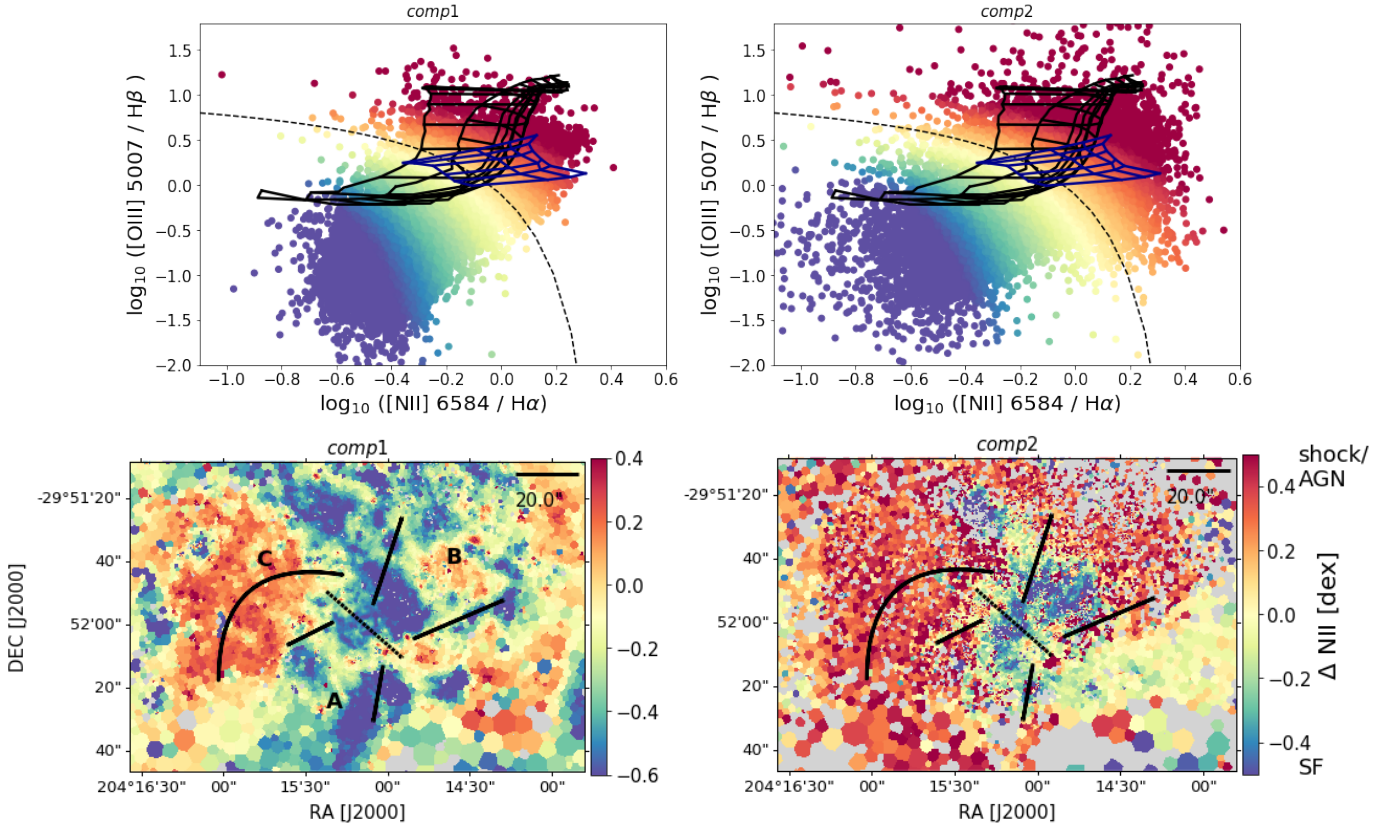


Fig. 15. N II-BPT diagrams obtained from a double component Gaussian fit to the emission lines. The line and model grids in the top panels are the same as in Fig. 8. Each Voronoi bin is colour coded according to its orthogonal distance from the extreme starburst line (Δ N II), ranging from blue (pure SF) to red (pure shock or AGN emission). Bins with an uncertainty $>50\%$ on either line ratio are excluded from the top plots. In the bottom plots, black lines mark the kinematic features discussed in Sect. 6.

alone would be difficult to reconcile with the large separation between the two peaks of $H\alpha$ emission (up to 200 km s^{-1}) at the centre of the cones.

In the near future, the increasing availability of IFS datasets comparable to the present study, covering large portions of local spiral galaxies at intermediate to high resolution, will allow for a better understanding of the signatures imprinted on the ionised gas by in- and outflows, as well as the relative importance of extraplanar gas in low inclination spirals.

7.2. Origin of the DIG

In Sect. 5 we separated the $H\alpha$ emission in our FoV into compact H II regions and diffuse ionised gas, finding a DIG fraction $f_{\text{DIG}} \sim 13\%$ (20%) based on a cut in $H\alpha$ surface brightness ($[\text{S II}]/H\alpha$ line ratio). This fraction is on the low end of the range with respect to observations in nearby spiral galaxies, where it was constrained to be between 30 and 50% (Ferguson et al. 1996; Hoopes et al. 1996; Zurita et al. 2000; Thilker et al. 2002; Belfiore et al. 2022), and in some cases even up to 60% (Oey et al. 2007). This might be due to the fact that the MUSE data only cover the inner portion of the optical disk ($R \leq 1.1 R_e$). The wide field spectrograph data by Poetrodjojo et al. (2019) imaging most of the optical disk ($R \leq 2 R_e$ at our assumed distance and R_e) revealed indeed that the DIG contribution increases (up to 40%) in the outskirts of the disk. Overall, we observe that despite the enhanced ratios of [N II], [S II] and [O I] with respect to $H\alpha$, 94.9% of the $H\alpha$ luminosity in the DIG is consistent with originating from star formation (BPT

diagrams in Figs. 8 and 9). This could support the hypothesis that the diffuse gas is for most part ionised by radiation escaping the SF regions. DIG featuring stronger ratios of $[\text{N II}]/H\alpha$, $[\text{S II}]/H\alpha$ can instead be partially explained with being extraplanar, as observed by Boettcher et al. (2017). The [N II] and [S II]/ $H\alpha$ ratios are indeed known to increase with distance from the galactic midplane (Madsen et al. 2006; Jones et al. 2017; Levy et al. 2019), due for example to shocks (Rand 1998), turbulent mixing layers (Rand 1998; Collins & Rand 2001) or ionisation by hot, old, low-mass evolved stars (HOLMES, Lacerda et al. 2018; Levy et al. 2019; Weber et al. 2019). We will investigate the origin of the diffuse ionised gas in more detail in a second publication (Della Bruna et al., in prep.).

8. Conclusions

We have presented a large MUSE mosaic covering the central $3.8 \text{ kpc} \times 3.8 \text{ kpc}$ of the nearby barred spiral galaxy M83 with a spatial resolution $\sim 20 \text{ pc}$. We obtained the kinematics of the stars and the ionised gas, and compared them with molecular gas kinematics from ALMA CO(2-1). We observed that the stellar kinematics trace regular rotation along the main SF disk, plus a fast rotating circumnuclear disk of $30''$ ($\simeq 700 \text{ pc}$) in diameter, likely originating from secular processes driven by the galactic bar.

The gas kinematics are rich in substructures, and the ionised and molecular gas substantially match one another. At large scales, the gas maps rotation along the disk, as well as the fast rotating circumnuclear disk component. On top of the disk

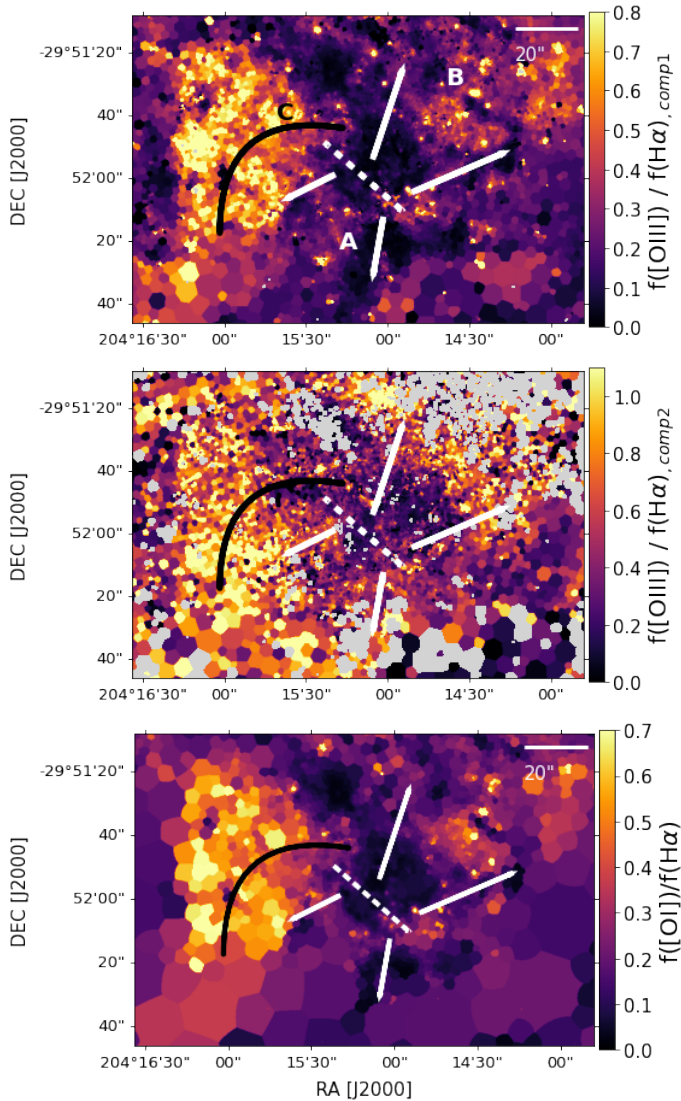


Fig. 16. Ratios of strong emission lines observed with MUSE. *Top and centre:* map of $[\text{O III}] \lambda 4959,5007/\text{H}\alpha$ obtained from a double component Gaussian fit to the emission lines. *Bottom panel:* map of $[\text{O I}] \lambda 6300/\text{H}\alpha$ obtained from a single Gaussian component fit. All maps have been corrected for extinction. The labelled features are discussed in Sect. 6.3. Maps of the full FoV are shown in Fig. B.2.

rotation, the gas traces a flow east of the nucleus ($50'' \approx 1250$ pc in size), that appears redshifted on top of the disk rotation. In the ionised gas, we observe $\Delta v_{\text{H}\alpha} \approx +30 \text{ km s}^{-1}$ with respect to the surroundings, and in the molecular gas we observe multiple peaks of emission, one of which is redshifted by $\Delta v_{\text{CO}} \approx +100 \text{ km s}^{-1}$ with respect to the emission tracing galactic rotation. We also observe an enhanced velocity dispersion both in the ionised gas ($\sigma_{\text{H}\alpha} \approx 80 \text{ km s}^{-1}$) and molecular gas ($\sigma_{\text{CO}} \approx 25 \text{ km s}^{-1}$ for the redshifted peak). The ionised gas showcases an extended region ($\sim 1000 \times 1600$ pc) surrounding the flow, whose emission lies above the upper limit for star formation in a N2-BPT emission line diagram, and is in large part consistent with models of slow shocks. The extended region also features high ratios of $[\text{O III}]/\text{H}\alpha$ (≥ 0.5) and $[\text{O I}]/\text{H}\alpha$ (≥ 0.5), indicative of a high ionisation state and of the presence shocks. We interpreted this feature as either the superposition of non-collisional flows originating from multiple vertical layers of gas or a bar-driven inflow of shocked gas.

A double component Gaussian fit to the $\text{H}\alpha$ line moreover revealed the presence of two distinct cone-shaped velocity components ($20'' \approx 500$ pc in size) on either side of the stellar bar, where the line features two distinct peaks that are up to 200 km s^{-1} apart. The two cones appear blue- and redshifted along our line of sight, with $v = \pm 100 \text{ km s}^{-1}$ and have a velocity dispersion $> 80 \text{ km s}^{-1}$ and up to 200 km s^{-1} . At the far end of both cones, the gas emission lies above the star formation limit in a N2-BPT diagram, in an area of the diagram consistent with slow shock models, and features an enhanced $[\text{O III}]/\text{H}\alpha$ ratio (≥ 0.4 in one or – in the case of cone B – in both of the Gaussian components). One of the two cones also features enhanced $[\text{O I}]/\text{H}\alpha$ ratios (≥ 0.4). We postulate that these two components are tracing a starburst-driven outflow perpendicular to the stellar bar, shocking into the surrounding ISM.

We estimated the gas extinction from the MUSE $\text{H}\beta/\text{H}\alpha$ ratio, and found that the regions more strongly affected by extinction ($E(B - V) > 0.5$) in general have a high density of molecular gas ($> 100 M_{\odot} \text{ pc}^{-2}$). Finally, we separated the ionised gas into H II regions and DIG, using a cut in $\text{H}\alpha$ surface brightness ($S_{\text{H}\alpha}/\text{H}\alpha$ line ratio). We obtained a DIG fraction $f_{\text{DIG}} \sim 13\%$ (20%) in our FoV, and observed that the DIG contribution varies radially between 0.8 and 46%, peaking in the interarm region (at $R \sim 0.3 R_e$). We inspected the emission of the H II regions and DIG in BPT diagrams, finding that in H II regions 99.8% of $L(\text{H}\alpha)$ originates from photoionisation-dominated regions, whereas the DIG has a mixed contribution from both photoionisation- (94.9%) and shock-dominated regions (5.1%).

Acknowledgements. We thank the anonymous referee for their very detailed and helpful feedback on this manuscript. We thank Jeff Rich and Lisa Kewley for sharing with us the slow shock models presented in Rich et al. (2011). This work is based on observations collected at the European Southern Observatory under ESO programmes 096.B-0057(A), 0101.B-0727(A), 097.B-0899(B), 097.B-0640(A). A.A. acknowledges the support of the Swedish Research Council, Vetenskapsrådet, and the Swedish National Space Agency (SNSA). F.R. acknowledges support from the Knut and Alice Wallenberg Foundation. This research made use of Astropy (<http://www.astropy.org>), a community-developed core Python package for Astronomy (Astropy Collaboration 2013, 2018).

References

- Adamo, A., Kruijssen, J. M. D., Bastian, N., Silva-Villa, E., & Ryon, J. 2015, *MNRAS*, **452**, 246
- Allen, M. G., Groves, B. A., Dopita, M. A., Sutherland, R. S., & Kewley, L. J. 2008, *ApJS*, **178**, 20
- Astropy Collaboration (Robitaille, T. P., et al.) 2013, *A&A*, **558**, A33
- Astropy Collaboration (Price-Whelan, A. M., et al.) 2018, *AJ*, **156**, 123
- Bacon, R., Accardo, M., Adjali, L., et al. 2010, in *The MUSE second-generation VLT instrument*, SPIE Conf. Ser., 7735, 773508
- Baldwin, J. A., Phillips, M. M., & Terlevich, R. 1981, *PASP*, **93**, 5
- Barrera-Ballesteros, J. K., Utomo, D., Bolatto, A. D., et al. 2020, *MNRAS*, **492**, 2651
- Belfiore, F., Santoro, F., Groves, B., et al. 2022, *A&A*, **659**, A26
- Bik, A., Östlin, G., Menacho, V., et al. 2018, *A&A*, **619**, A131
- Binney, J., & Tremaine, S. 1987, *Galactic Dynamics* (Princeton, N.J: Princeton University Press)
- Bizyaev, D., Walterbos, R. A. M., Yoachim, P., et al. 2017, *ApJ*, **839**, 87
- Blair, W. P., Chandar, R., Dopita, M. A., et al. 2014, *ApJ*, **788**, 55
- Boettcher, E., Gallagher, J. S. I., & Zweibel, E. G. 2017, *ApJ*, **845**, 155
- Bohlin, R. C., Savage, B. D., & Drake, J. F. 1978, *ApJ*, **224**, 132
- Bolatto, A. D., Wolfire, M., & Leroy, A. K. 2013, *ARA&A*, **51**, 207
- Bresolin, F., Kudritzki, R.-P., Urbaneja, M. A., et al. 2016, *ApJ*, **830**, 64
- Bryant, J. J., Owers, M. S., Robotham, A. S. G., et al. 2015, *MNRAS*, **447**, 2857
- Bundy, K., Bershady, M. A., Law, D. R., et al. 2015, *ApJ*, **798**, 7
- Buta, R., & Crocker, D. A. 1993, *AJ*, **105**, 1344
- Buta, R. J., Sheth, K., Athanassoula, E., et al. 2015, *ApJS*, **217**, 32

- Callanan, D., Longmore, S. N., Kruijssen, J. M. D., et al. 2021, *MNRAS*, 505, 4310
- Calzetti, D., Harris, J., Gallagher, J. S. I., et al. 2004, *AJ*, 127, 1405
- Cappellari, M. 2017, *MNRAS*, 466, 798
- Cappellari, M., & Copin, Y. 2003, *MNRAS*, 342, 345
- Cappellari, M., & Emsellem, E. 2004, *PASP*, 116, 138
- Cardelli, J. A., Clayton, G. C., & Mathis, J. S. 1989, *ApJ*, 345, 245
- Collins, J. A., & Rand, R. J. 2001, *ApJ*, 551, 57
- Comerón, S., Knapen, J. H., Beckman, J. E., et al. 2010, *MNRAS*, 402, 2462
- Croom, S. M., Lawrence, J. S., Bland-Hawthorn, J., et al. 2012, *MNRAS*, 421, 872
- Dale, J. E. 2015, *New Astron. Rev.*, 68, 1
- Dale, J. E., Ngoumou, J., Ercolano, B., & Bonnell, I. A. 2014, *MNRAS*, 442, 694
- Della Bruna, L., Adamo, A., Bik, A., et al. 2020, *A&A*, 635, A134
- Della Bruna, L., Adamo, A., Lee, J. C., et al. 2021, *A&A*, 650, A103
- den Brok, M., Carollo, C. M., Erroz-Ferrer, S., et al. 2020, *MNRAS*, 491, 4089
- den Brok, J. S., Chatzigiannakis, D., Bigiel, F., et al. 2021, *MNRAS*, 504, 3221
- de Vaucouleurs, G., de Vaucouleurs, A., Corwin, H. G. J., et al. 1991, *Third Reference Catalogue of Bright Galaxies* (New York: Springer)
- Díaz, R. J., Dottori, H., Agüero, M. P., et al. 2006, *ApJ*, 652, 1122
- Diehl, S., & Statler, T. S. 2006, *MNRAS*, 368, 497
- Draine, B. T. 2011, *Physics of the Interstellar and Intergalactic Medium* (Princeton University Press)
- Drissen, L., Martin, T., Rousseau-Nepton, L., et al. 2019, *MNRAS*, 485, 3930
- Elmegreen, D. M., Chromey, F. R., & Warren, A. R. 1998, *AJ*, 116, 2834
- Emsellem, E. 2004, in *Coevolution of Black Holes and Galaxies*, ed. L. C. Ho, 11
- Emsellem, E., Greusard, D., Combes, F., et al. 2001, *A&A*, 368, 52
- Emsellem, E., Renaud, F., Bournaud, F., et al. 2015, *MNRAS*, 446, 2468
- Emsellem, E., Schinnerer, E., Santoro, F., et al. 2022, *A&A*, 659, A191
- Epinat, B., Amram, P., Marcelin, M., et al. 2008, *MNRAS*, 388, 500
- Erroz-Ferrer, S., Carollo, C. M., den Brok, M., et al. 2019, *MNRAS*, 484, 5009
- Farage, C. L., McGregor, P. J., Dopita, M. A., & Bicknell, G. V. 2010, *ApJ*, 724, 267
- Fathi, K., Beckman, J. E., Lundgren, A. A., et al. 2008, *ApJ*, 675, L17
- Ferguson, A. M. N., Wyse, R. F. G., Gallagher, J. S. I., & Hunter, D. A. 1996, *AJ*, 111, 2265
- Gadotti, D. A., Sánchez-Blázquez, P., Falcón-Barroso, J., et al. 2019, *MNRAS*, 482, 506
- Gadotti, D. A., Bittner, A., Falcón-Barroso, J., et al. 2020, *A&A*, 643, A14
- Gaia Collaboration (Brown, A. G. A., et al.) 2018, *A&A*, 616, A1
- Girardi, L., Bressan, A., Bertelli, G., & Chiosi, C. 2000, *A&AS*, 141, 371
- Guérou, A., Krajinović, D., Epinat, B., et al. 2017, *A&A*, 608, A5
- Hadfield, L. J., Crowther, P. A., Schild, H., & Schmutz, W. 2005, *A&A*, 439, 265
- Haffner, L. M., Dettmar, R. J., Beckman, J. E., et al. 2009, *Rev. Mod. Phys.*, 81, 969
- Heald, G., de Blok, W. J. G., Lucero, D., et al. 2016, *MNRAS*, 462, 1238
- Hoopes, C. G., & Walterbos, R. A. M. 2000, *ApJ*, 541, 597
- Hoopes, C. G., & Walterbos, R. A. M. 2003, *ApJ*, 586, 902
- Hoopes, C. G., Walterbos, R. A. M., & Greenwalt, B. E. 1996, *AJ*, 112, 1429
- Hopkins, P. F., Narayanan, D., & Murray, N. 2013, *MNRAS*, 432, 2647
- Hopkins, P. F., Wetzel, A., Kereš, D., et al. 2018, *MNRAS*, 480, 800
- Houghton, R. C. W., & Thatte, N. 2008, *MNRAS*, 385, 1110
- Howard, C. S., Pudritz, R. E., & Harris, W. E. 2017, *MNRAS*, 470, 3346
- Jacobs, B. A., Rizzi, L., Tully, R. B., et al. 2009, *AJ*, 138, 332
- Jones, A., Kauffmann, G., D'Souza, R., et al. 2017, *A&A*, 599, A141
- Kamann, S. 2018, *PampelMuse: Crowded-field 3D Spectroscopy* (Astrophysics Source Code Library)
- Kauffmann, G., Heckman, T. M., Tremonti, C., et al. 2003, *MNRAS*, 346, 1055
- Kewley, L. J., Dopita, M. A., Sutherland, R. S., Heisler, C. A., & Trevena, J. 2001, *ApJ*, 556, 121
- Kewley, L. J., Nicholls, D. C., & Sutherland, R. S. 2019, *ARA&A*, 57, 511
- Knapen, J. H., Sharp, R. G., Ryder, S. D., et al. 2010, *MNRAS*, 408, 797
- Koch, E. W., Rosolowsky, E. W., Leroy, A. K., et al. 2021, *MNRAS*, 504, 1801
- Kreckel, K., Blanc, G. A., Schinnerer, E., et al. 2016, *ApJ*, 827, 103
- Kreckel, K., Ho, I. T., Blanc, G. A., et al. 2019, *ApJ*, 887, 80
- Krumholz, M. R., & Kruijssen, J. M. D. 2015, *MNRAS*, 453, 739
- Krumholz, M. R., Bate, M. R., Arce, H. G., et al. 2014, in *Protostars and Planets VI*, eds. H. Beuther, R. S. Klessen, C. P. Dullemond, & T. Henning, 243
- Krumholz, M. R., Kruijssen, J. M. D., & Crocker, R. M. 2017, *MNRAS*, 466, 1213
- Lacerda, E. A. D., Cid Fernandes, R., Couto, G. S., et al. 2018, *MNRAS*, 474, 3727
- Leroy, A. K., Bolatto, A. D., Ostriker, E. C., et al. 2015a, *ApJ*, 801, 25
- Leroy, A. K., Walter, F., Martini, P., et al. 2015b, *ApJ*, 814, 83
- Leroy, A. K., Schinnerer, E., Hughes, A., et al. 2021a, *ApJS*, 257, 43
- Leroy, A. K., Hughes, A., Liu, D., et al. 2021b, *ApJS*, 255, 19
- Leroy, A. K., Rosolowsky, E., Usero, A., et al. 2022, *ApJ*, 927, 149
- Levy, R. C., Bolatto, A. D., Sánchez, S. F., et al. 2019, *ApJ*, 882, 84
- Lundgren, A. A., Olofsson, H., Wiklund, T., & Rydbeck, G. 2004, *A&A*, 422, 865
- Luridiana, V., Morisset, C., & Shaw, R. A. 2015, *A&A*, 573, A42
- Madsen, G. J., Reynolds, R. J., & Haffner, L. M. 2006, *ApJ*, 652, 401
- Maiolino, R., & Mannucci, F. 2019, *A&ARv*, 27, 3
- Makarov, D., Prugniel, P., Terekhova, N., Courtois, H., & Vauglin, I. 2014, *A&A*, 570, A13
- Martins, F., Schaerer, D., & Hillier, D. J. 2005, *A&A*, 436, 1049
- Mast, D., Díaz, R. J., & Agüero, M. P. 2006, *AJ*, 131, 1394
- McLeod, A. F., Dale, J. E., Evans, C. J., et al. 2019, *MNRAS*, 486, 5263
- McLeod, A. F., Kruijssen, J. M. D., Weisz, D. R., et al. 2020, *ApJ*, 891, 25
- McLeod, A. F., Ali, A. A., Chevance, M., et al. 2021, *MNRAS*, 508, 5425
- Miller, E. D., Bregman, J. N., & Wakker, B. P. 2009, *ApJ*, 692, 470
- Morisset, C., Delgado-Inglada, G., Sánchez, S. F., et al. 2016, *A&A*, 594, A37
- Oey, M. S., Meurer, G. R., Yelda, S., et al. 2007, *ApJ*, 661, 801
- Osterbrock, D. E., & Ferland, G. J. 2006, *Astrophysics of Gaseous Nebulae and Active Galactic Nuclei* (Sausalito, CA: University Science Books)
- Patule, G., Petit, C., Prugniel, P., et al. 2003, *A&A*, 412, 45
- Piqueras López, J., Davies, R., Colina, L., & Orban de Xivry, G. 2012, *ApJ*, 752, 47
- Plummer, H. C. 1911, *MNRAS*, 71, 460
- Poetrodjojo, H., D'Agostino, J. J., Groves, B., et al. 2019, *MNRAS*, 487, 79
- Popesso, P., Concas, A., Morselli, L., et al. 2019, *MNRAS*, 483, 3213
- Rand, R. J. 1998, *ApJ*, 501, 137
- Rautio, R. P. V., Watkins, A. E., Comerón, S., et al. 2022, *A&A*, 659, A153
- Regan, M. W., & Teuben, P. 2003, *ApJ*, 582, 723
- Renaud, F., Bournaud, F., Emsellem, E., et al. 2015, *MNRAS*, 454, 3299
- Rich, J. A., Kewley, L. J., & Dopita, M. A. 2011, *ApJ*, 734, 87
- Rodrigues, I., Dottori, H., Díaz, R. J., Agüero, M. P., & Mast, D. 2009, *AJ*, 137, 4083
- Rosolowsky, E., Hughes, A., Leroy, A. K., et al. 2021, *MNRAS*, 502, 1218
- Rossa, J., & Dettmar, R. J. 2003, *A&A*, 406, 493
- Rousseau-Nepton, L., Martin, R. P., Robert, C., et al. 2019, *MNRAS*, 489, 5530
- Russell, T. D., White, R. L., Long, K. S., et al. 2020, *MNRAS*, 495, 479
- Salo, H., Laurikainen, E., Laine, J., et al. 2015, *ApJS*, 219, 4
- Sánchez, S. F., Kennicutt, R. C., Gil de Paz, A., et al. 2012, *A&A*, 538, A8
- Sánchez, S. F., Pérez, E., Rosales-Ortega, F. F., et al. 2015, *A&A*, 574, A47
- Sandstrom, K. M., Leroy, A. K., Walter, F., et al. 2013, *ApJ*, 777, 5
- Scannapieco, C., Wadepuhl, M., Parry, O. H., et al. 2012, *MNRAS*, 423, 1726
- Schaye, J., Crain, R. A., Bower, R. G., et al. 2015, *MNRAS*, 446, 521
- Schwarz, G. 1978, *Ann. Stat.*, 6, 461
- Seon, K.-I., & Witt, A. N. 2012, *ApJ*, 758, 109
- Sérsic, J. L., & Pastoriza, M. 1965, *PASP*, 77, 287
- Sheth, K., Regan, M., Hinz, J. L., et al. 2010, *PASP*, 122, 1397
- Shopbell, P. L., & Bland-Hawthorn, J. 1998, *ApJ*, 493, 129
- Silva-Villa, E., Adamo, A., Bastian, N., Fouesneau, M., & Zackrisson, E. 2014, *MNRAS*, 440, L116
- Simkin, S. M., Su, H. J., & Schwarz, M. P. 1980, *ApJ*, 237, 404
- Sun, J., Leroy, A. K., Schinnerer, E., et al. 2020, *ApJ*, 901, L8
- Thatte, N., Tecza, M., & Genzel, R. 2000, *A&A*, 364, L47
- Thilker, D. A., Walterbos, R. A. M., Braun, R., & Hoopes, C. G. 2002, *AJ*, 124, 3118
- Vandenbroucke, B., Wood, K., Girichidis, P., Hill, A. S., & Peters, T. 2018, *MNRAS*, 476, 4032
- Vazdekis, A., Koleva, M., Ricciardelli, E., Röck, B., & Falcón-Barroso, J. 2016, *MNRAS*, 463, 3409
- Veilleux, S., & Osterbrock, D. E. 1987, *ApJS*, 63, 295
- Warner, P. J., Wright, M. C. H., & Baldwin, J. E. 1973, *MNRAS*, 163, 163
- Weber, J. A., Pauldrach, A. W. A., & Hoffmann, T. L. 2019, *A&A*, 622, A115
- Weilbacher, P. M., Streicher, O., Urrutia, T., et al. 2014, in *Astronomical Data Analysis Software and Systems XXIII*, eds. N. Manset, & P. Forshay, *ASP Conf. Ser.*, 485, 451
- Weilbacher, P. M., Monreal-Ibero, A., Verhamme, A., et al. 2018, *A&A*, 611, A95
- Weilbacher, P. M., Palsa, R., Streicher, O., et al. 2020, *A&A*, 641, A28
- Williams, B. F., Hillis, T. J., Blair, W. P., et al. 2019, *ApJ*, 881, 54
- Winkler, P. F., Blair, W. P., & Long, K. S. 2017, *ApJ*, 839, 83
- Wood, K., & Mathis, J. S. 2004, *MNRAS*, 353, 1126
- Yukita, M., Hornschemeier, A. E., Lehmer, B. D., et al. 2016, *ApJ*, 824, 107
- Zhang, K., Yan, R., Bundy, K., et al. 2017, *MNRAS*, 466, 3217
- Zurita, A., Rozas, M., & Beckman, J. E. 2000, *A&A*, 363, 9
- Zurita, A., Beckman, J. E., Rozas, M., & Ryder, S. 2002, *A&A*, 386, 801

Appendix A: Additional material on the kinematics fitting analysis

A.1. Rotation curves and 2D velocity fields

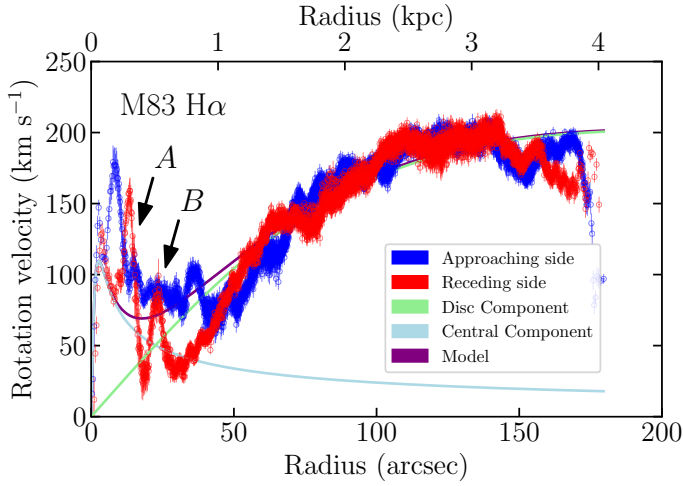


Fig. A.1. Same as the middle panel of Fig. 4, but for model (e) in Table 2, which enforces a symmetrical curve.

In Fig. A.1 we present the rotation curve for model (e) (same as in Fig. 4 but enforcing $\Delta V_{\text{rot}} = 0$). In Fig. A.2 we show two-dimensional (2D) residual velocity fields for the best-fit models, (A) and (a), respectively. 2D-residual fields are used to optimise the free parameter determination of the rotation curves that are computed from 2D-velocity fields. The residual velocity fields (V_{res}) shown in the figure are obtained after subtracting the best fit models (models (A) and (a) reported in Table 2) from the observed velocity field. Because rotation curves are based on axisymmetric models, specific patterns observed on the residual velocity field would be due to an incorrect parameter determination (Warner et al. 1973). As a consequence, when the free parameters of the rotation curve are optimised, the residual velocity field is typical-pattern-free and the amplitude in the 2D residual velocity is minimum. No artefacts are observed in

the residual velocity fields, indicating that the models are optimal. The main residual patterns that remain are due to non-axisymmetric features (e.g. the large-scale spiral structure and the central component which features an asymmetric X-shape pattern).

A.2. Uncertainty estimation

The raw stellar LoS velocity field consists of 1,678,471 velocity measurements. To remove spaxels possibly containing spurious information, the raw stellar field was masked accounting for spaxels with low S/N and/or large errors in the velocity or velocity dispersion determination, which resulted in masking of 0.16% of the spaxels. Despite the nine free parameters, due to the large number of spaxels used in the fit, the associated statistical uncertainties are very low. Therefore, in order to study the robustness of the fit we inspect three additional models for which we set centre locations estimated in the literature. Fig. A.3 shows these locations, all found within a box of $\sim 3 \times 3$ arcsec², close to the brightest central clumps of M83. For models (B), (C) and (D) we fix the centre to the coordinates computed in two different studies for which uncertainties have been computed. In model (B), we utilise the kinematic centre computed by Fathi et al. (2008) that used the H α line and 2D-spectroimagery (Fabry-Perot); for model (C) we use the one determined by Knapen et al. (2010) from kinematic Pa β data. Finally, to estimate our own uncertainty on the centre, for model (D) we consider the corner of the uncertainty box for Knapen et al. (2010) (grey box in Fig. A.3) that is the furthest away from the centre determined in model (A). The fits lead to very similar parameters (see table 2). Even if model (A) provides the smallest χ_r^2 , model (B) cannot be discarded just on the relevance of its χ_r^2 which is only less than 2% higher than those of model (A). Model (C) and (D) lead to χ_r^2 respectively 5 and 12% larger than model (A). In conclusion we can estimate that our centre uncertainty within a χ_r^2 variation of 2% is $\Delta\alpha \pm 4$ arcsec and $\Delta\delta \pm 1$ arcsec. We observe that the disagreement in the rotation curves between the approaching and receding sides within the first kpc - and especially within the first 100 pc - becomes increasingly large with models (B), (C) and (D), confirming that model (A) is the best fit.

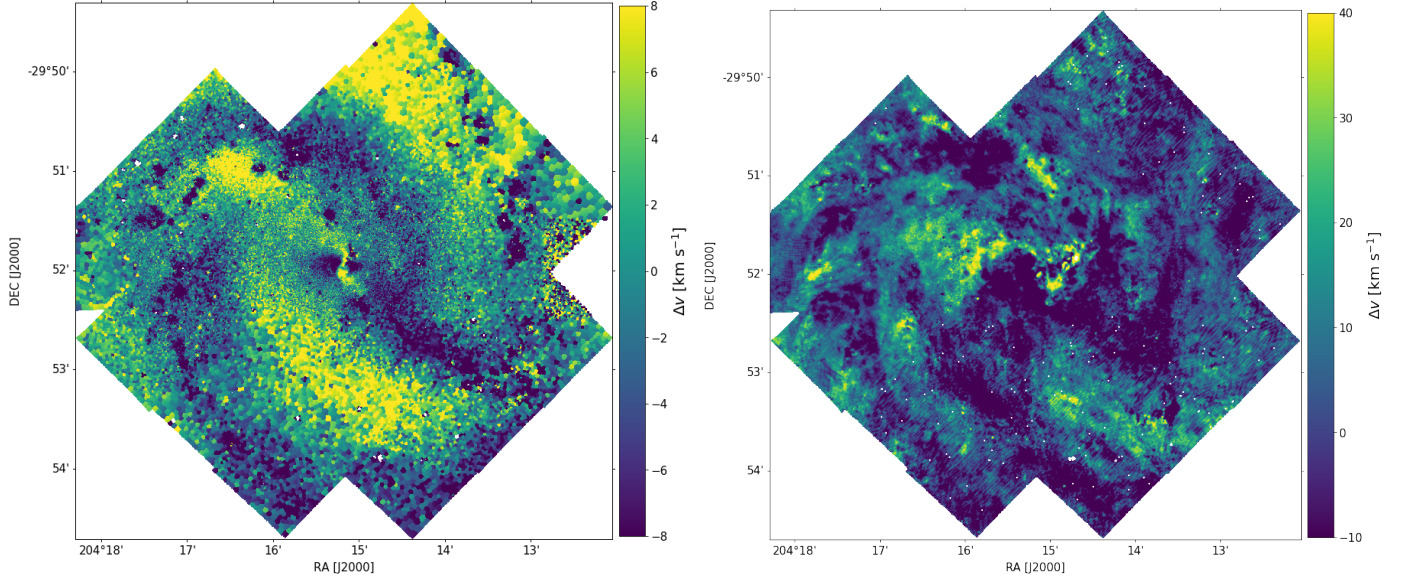


Fig. A.2. 2D residual velocity for model (A) (left) and (d) (right), as described in Table 2.

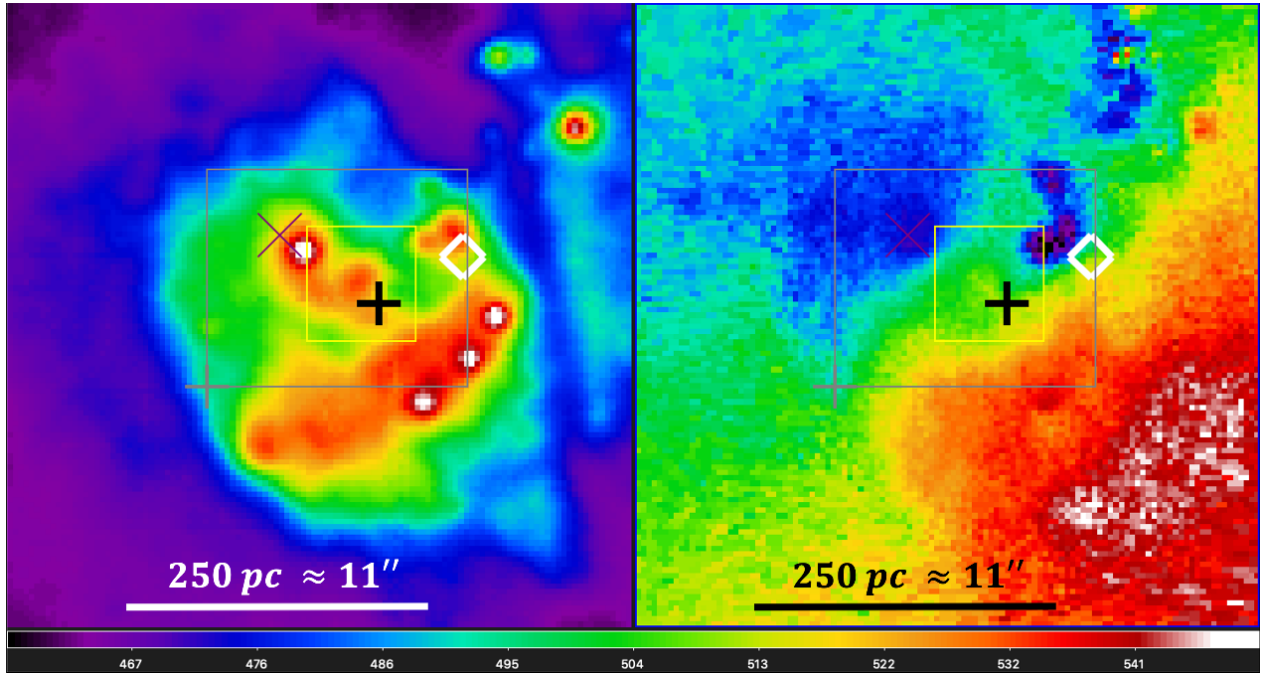


Fig. A.3. Different centre positions from this work and the literature. Boxes indicate uncertainty determinations from centres as calculated by other authors. The background images show: continuum emission around the $H\alpha$ line, rescaled in intensity (left panel, arbitrary units) and the observed stellar velocity field (right panel and horizontal colour bar, not corrected for the systemic velocity). The coordinates of the symbols and the box centres are given in Table A.1. Yellow box (Fabry-Perot kinematic centre, Fathi et al. 2008, Knapen et al. 2010, size of the box: 4.0×4.2 arcsec²); grey box (Pa β kinematic centre, Knapen et al. 2010, size of the box: 9.6×8.0 arcsec²); grey '+' (corner of the Pa β uncertainty box that is the furthest away from the centre determined using the MUSE stellar velocity map); purple 'X' (optical nucleus, Díaz et al. 2006); white '◇' (MUSE stellar kinematic centre from model (A), this work); black '+' (CO kinematic centre from model (β), this work).

Table A.1. Centre positions from this work and the literature shown in Fig. A.3.

Centre	RA (J2000)	DEC (J2000)	Symbol	Ref
MUSE stellar kinematic centre (model (A))	13:37:00.43	-29:51:56.2	white '◇'	This work
CO kinematic centre (model (β))	13:37:01.14	-29:51:52.5	black '+'	This work
Fabry-Perot kinematic centre	13:37:00.75	-29:51:57.3	yellow box	(1), (2)
Pa β kinematic centre	13:37:00.81	-29:51:57.1	grey box	(2)
Outermost Pa β centre ^(a)	13:37:01.13	-29:51:59.5	grey '+'	(3)
Optical nucleus	13:37:00.95	-29:51:55.5	purple 'X'	(3), (2)

Notes. ^aMaximum distance to the MUSE stellar kinematic centre within the uncertainty on the Pa β centre.

References. (1) Fathi et al. (2008); (2) Knapen et al. (2010); (3) Díaz et al. (2006).

Appendix B: Supplementary linemaps

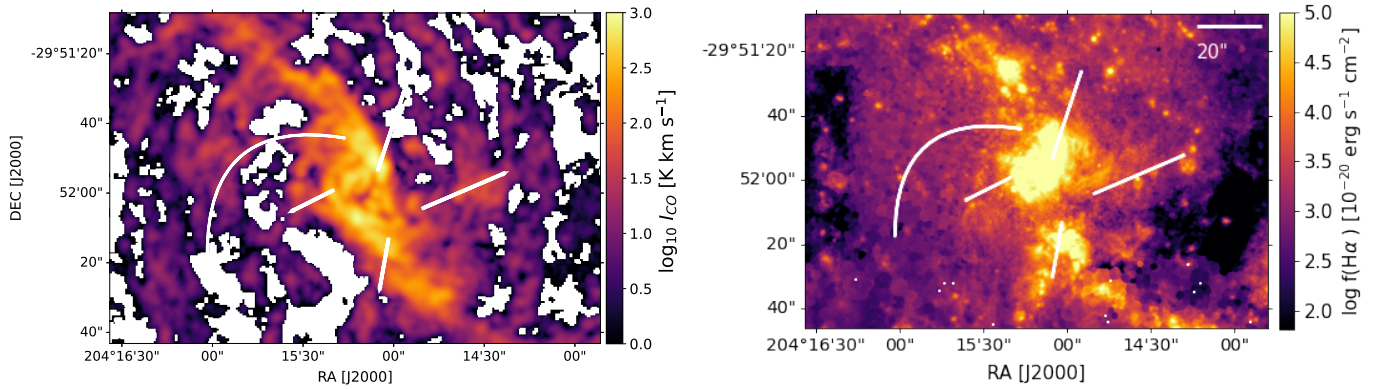


Fig. B.1. Central starburst region observed in ALMA CO(2-1) (left panel) and in MUSE H α (reddening corrected, right panel). The white lines mark the position of the features discussed in Sect. 6.

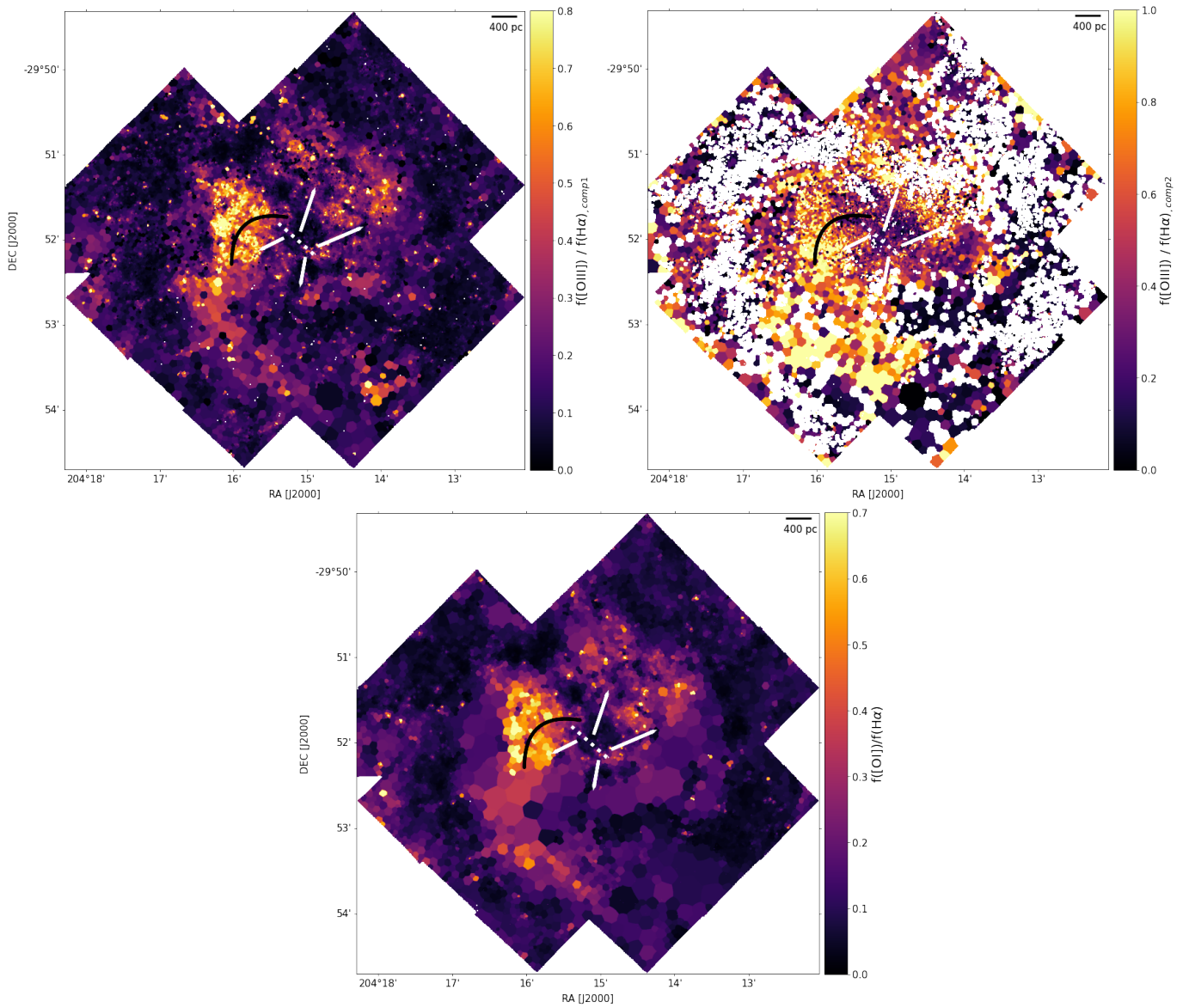


Fig. B.2. Same as Fig. 16, but for the full FoV.

Appendix C: MUSE dataset coverage and properties**Table C.1.** Central coordinates, exposure time, and seeing of the MUSE mosaic tiles. The seeing has been measured at 7000 Å, as described in Sect. 2.

ID	Programme ID	RA (J2000)	DEC (J2000)	$t_{\text{exp,tot}}$ [s]	Seeing [arcsec]
Pnt1	096.B-0057(A)	13:37:00.4900	-29:52:00.300	2750	0.72
Pnt2	096.B-0057(A)	13:37:03.6200	-29:51:21.700	2200	0.77
Pnt3	096.B-0057(A)	13:37:00.5000	-29:50:41.100	2200	0.80
Pnt4	096.B-0057(A)	13:36:57.4500	-29:51:20.600	2750	0.80
Pnt5	096.B-0057(A), 0101.B-0727(A)	13:37:06.6600	-29:52:00.300	2200	0.81
Pnt6	096.B-0057(A), 0101.B-0727(A)	13:37:09.7000	-29:52:39.900	2200	0.84
Pnt7	096.B-0057(A), 0101.B-0727(A)	13:37:09.7100	-29:51:20.700	2200	0.68
Pnt8	096.B-0057(A), 0101.B-0727(A)	13:37:06.6700	-29:50:41.100	2200	0.73
Pnt9	096.B-0057(A)	13:37:03.6200	-29:52:39.900	550	0.63
Pnt10	096.B-0057(A)	13:37:06.6600	-29:53:19.500	550	0.91
Pnt11	096.B-0057(A)	13:37:03.6100	-29:53:59.100	550	0.73
Pnt12	096.B-0057(A)	13:37:00.5700	-29:53:19.400	550	0.67
Pnt13	096.B-0057(A)	13:36:57.5300	-29:52:39.900	550	0.73
Pnt14	096.B-0057(A)	13:36:57.5200	-29:53:59.100	550	0.57
Pnt15	096.B-0057(A)	13:36:54.4800	-29:53:19.400	550	0.73
Pnt16	096.B-0057(A)	13:36:51.4400	-29:52:39.800	550	0.66
Pnt17	096.B-0057(A)	13:36:54.4800	-29:52:00.300	550	0.62
Pnt18	096.B-0057(A)	13:36:51.4400	-29:51:20.600	550	0.77
Pnt19	096.B-0057(A)	13:36:54.4900	-29:50:41.100	550	0.67
Pnt20	096.B-0057(A)	13:36:57.5300	-29:50:01.500	550	0.71
A1	097.B-0899(B)	13:36:58.2800	-29:51:55.900	1800	0.86
A2	097.B-0899(B)	13:36:53.7300	-29:51:57.100	1800	0.80
A3	097.B-0899(B)	13:37:02.7000	-29:51:55.500	1800	0.87
A4	097.B-0899(B)	13:37:07.2100	-29:51:54.600	1800	0.71
A7	097.B-0899(B)	13:37:11.7100	-29:51:53.700	1800	1.10
B1	097.B-0640(A)	13:37:00.8300	-29:51:55.500	1920	0.80

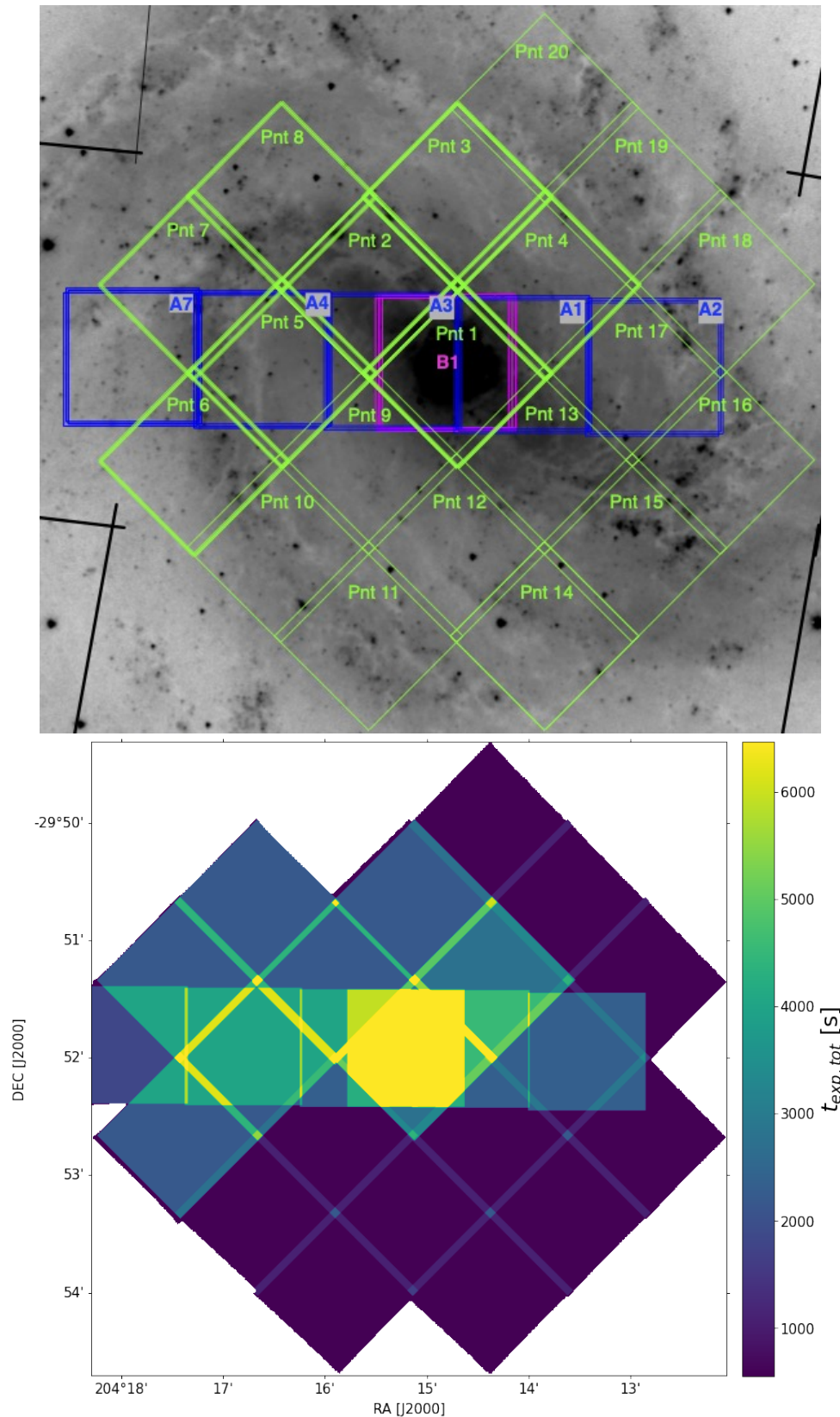


Fig. C.1. Layout of the MUSE mosaic. *Top panel:* location of the MUSE mosaic tiles. In green we indicate the data acquired as part of this project (PI Adamo); in blue and purple archival data that we have included in the final mosaic (PI Ibar and Gadotti). *Bottom panel:* total exposure time of each mosaic tile.